DESIGN REPORT

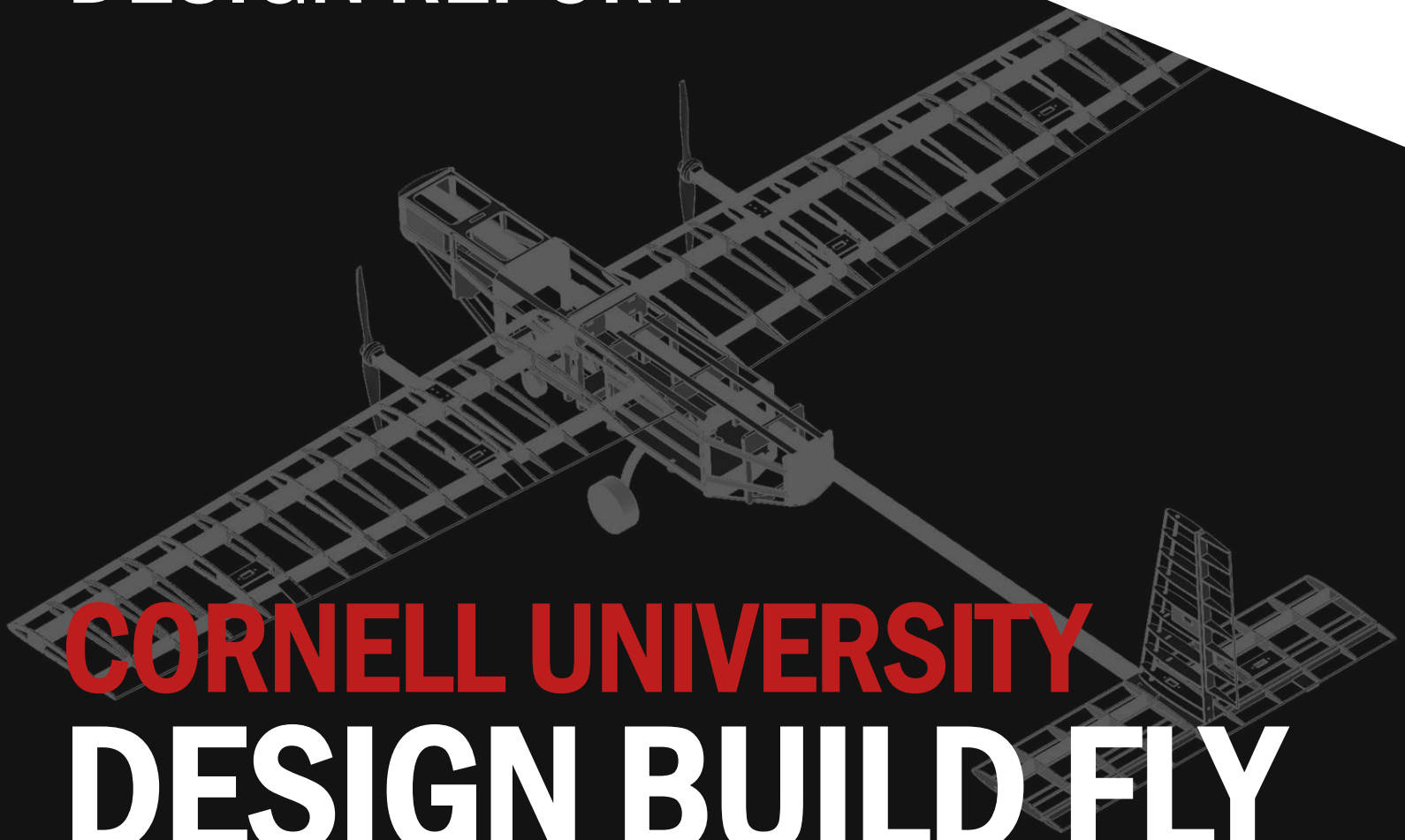

CORNELL UNIVERSITY
DESIGN BUILD FLY

2021-22

AIAA, TEXTRON, RAYTHEON

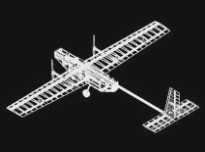

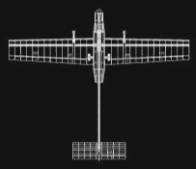

Table of Contents

§1 – Executive Summary 3
§2 – Management Summary 3
§2.1 – Team Organization 3
§2.2 – Operational Cadence and Communication Flow 4
§2.3 – Timeline and Milestones 5
§3 – Conceptual Design 6
§3.1 – Mission Requirements Decomposition 6
§3.1.1 – Ground Mission – Operational Demonstration 6
§3.1.2 – Mission 1 – Deployment Flight 6
§3.1.3 – Mission 2 – Staging Flight 7
§3.1.4 – Mission 3 – Vaccine Delivery Flight 7
§3.1.5 – Scoring 8
§3.2 – Design Parameters Sensitivity Analysis 8
§3.3 – Configuration Determination 9
§3.3.1 – Wing Configuration 9
§3.3.2 – Empennage Configuration 11
§3.3.3 – Propulsion Configuration 12
§3.3.4 – Fuselage Configuration 13
§3.3.5 – Landing Gear Configuration 13
§4 – Preliminary Design 14
§4.1 – Design and Analysis Methodology 14
§4.2 – Design and Sizing Trade Studies 15
§4.2.1 – Aircraft Sizing 15
§4.2.2 – Propulsion 17
§4.3 – Tail Sizing 21
§4.4 – Performance Predictions 22
§4.4.1 – Aircraft Performance 22
§4.4.2 – Aircraft Stability 24
§5 – Detailed Design 25
§5.1 – Subsystem Design 25
§5.1.1 – Propulsion 25
§5.1.2 – Fuselage 27
§5.1.3 – Landing Gear 28
§5.1.4 – *Wing* 29
§5.1.5 – Tail 32
§5.1.6 – Mission 2 Syringe Rack 34
§5.1.7 – Mission 3 Package Deployment Mechanism 35
§5.2 – Weight and Balance 36
§5.3 – Flight Performance Parameters 37
§5.4 – Mission Performance 39
§5.5 – Drawing Package 40
§6 – Manufacturing Plan 45
§6.1 – Manufacturing Workflow 45
§6.2 – Laser cutting 45
§6.3 – 3D printing 46
§6.4 – Landing Gear 46
§6.5 – MonoKote Covering 46
§6.6 – Adhesives 46
§6.7 – Wing 46
§6.8 – Fuselage 47
§6.9 – Tail 47
§6.10 – Competition Mechanisms 48
§7 – Testing Plan 48
§7.1 – Key Ground and Flight Tests 48
§7.1.1 – Mission 3 Pack*age Deployment Mechanism* 48
§7.1.2 – Landing Gear Testing 51
§7.1.3 – Fuselage Spar Finite Element Analysis 52
§7.1.4 – Wingtip Loading and Deflection 53
§7.1.5 – Propulsion Tests 55
§7.2 – Timeline and Schedule 56
§7.3 – Checklists 57
§8 – Performance Results 58
§8.1 - Static Thrust Testing 58
§8.2 - Wingtip Deflection Testing 58
§9 – Bibliography 60

§1 – Executive Summary

This document serves as the Cornell University Design Build Fly team's design report for the 2021-22 AIAA Design Build Fly competition, detailing the team's design, analysis, manufacture, and testing of a remote-controlled electric aircraft designed for humanitarian missions of vaccine delivery.

The aircraft was required to be capable of a deployment flight (Mission 1) with no payload, a staging flight (Mission 2) carrying a payload of syringes, and a vaccine delivery flight (Mission 3) consisting of several flights with remote deployment of sensitive vaccine vial packages within a specified drop area in between those flights. The mission score is a function of the number of syringes, total flight time, and number of Mission 3 package deployments.

A scoring sensitivity analysis revealed the mission score to be most significantly impacted by number of syringes, so the team prioritized increasing number of syringes that the aircraft could carry, though the importance of Mission 3 package deployments, flight time, and payload access were also recognized. The team's design was developed to reflect those priorities and is expected to be capable of carrying 30 syringes in Mission 2, as well as carrying and deploying 3 vaccine package payloads in Mission 3. The expected flight times for Missions 1 and 2 are 2.12 min, and 4.17 min for Mission 3 with a takeoff thrust of 39.4 N and a cruise (maximum) speed of 29 ms^{-1}.

The design consists of a streamlined payload-containing fuselage with hatches providing ease of access to the payload, a high wing of maximum allowable wingspan, a two-motor propulsion system, and a conventional empennage, all oriented around a pair of central structural carbon fiber spars – one along the wing and one along the fuselage. By maximizing wingspan and introducing flaps, the team was able to optimize maximum payload mass that could be carried while ensuring the vehicle could take off in the required distance. The carbon fiber structural spars are key in the design as they provide the rigidity needed to withstand the forces and moments exerted on an aircraft of such large dimensions. Three syringe brackets are used to constrain syringe movement during flight, with each securing ten syringes. The package deployment mechanism was developed as a rack and pinion system to drop packages out of the fuselage, with an additional elastic element ensuring the packages do not trip shock sensors by decelerating and redirecting packages as they are dropped from the fuselage.

The remainder of this design report document provides 1) an operational overview of the team, including team organization, a timeline, and a budget breakdown, 2) a discussion of the conceptual design process, including mission requirements decomposition, scoring sensitivity analysis, and initial configuration decisions, 3) elaboration on preliminary design, including design and analysis methodologies, as well as sizing studies, 4) detailed descriptions of and reasonings for subsystem designs, in addition to flight performance estimates and a CAD drawing package, 5) a discussion of the manufacturing and testing plans, including performance results.

§2 – Management Summary

§2.1 – Team Organization

Team leadership consists of two team leads, one primarily responsible for the technical direction of the team, guiding design decisions and aircraft development, and the other responsible for logistical aspects of the team's

operations, for example directing recruitment and managing scheduling. Additionally, a faculty advisor provides technical insight and feedback during design reviews.

The team is organized into four subteams, distinguished by responsibility and function, as depicted in Fig. 2.1.1, with 24 technical members involved in aircraft design as part of the Aerodynamics and Controls, Propulsion, or Mechanical subteams. Each technical subteam has two subteam leads, who are responsible for directing subteam level activities, ensuring relevant subsystem requirements are met, and interfacing with the team leads. The specific role of each subteam, and the individual skill sets required of members in each are presented in Table 2.1.1.

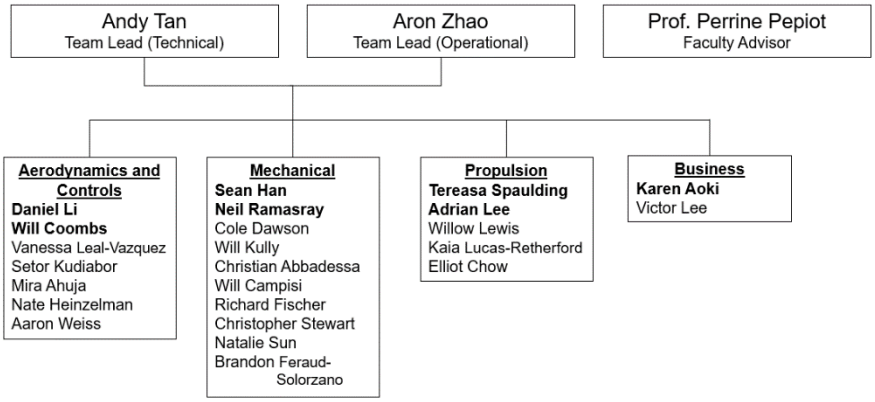

Fig. 2.1.1 - Team Organizational Structure

Table 2.1.1 – Subteam Responsibilities and Skillsets

Subteam	Responsibilities	Individual Skillsets
Aerodynamics and Controls	Responsible for optimization of flight performance as well as sizing and scoring analysis. Designs and integrates the following subsystems: Wing, Empennage, Control Surfaces	Understanding of aerodynamic theory, proficiency in SolidWorks and MATLAB, specialization in AVL, XFoil, or other aerodynamic analysis tool
Propulsion	Responsible for configuration selection, development, and integration of the following subsystems: Propulsion, Electrical/Controls	Understanding of motor, battery, and propellor selection using ECalc; proficiency in soldering and wiring with receivers, ESCs, servos, etc
Mechanical	Responsible for mechanisms and structures of the aircraft. Designs and integrates the following subsystems: Fuselage, Landing Gear, Mission-Specific Mechanism (Package Deployment)	Understanding of statics and mechanics of materials, proficiency in SolidWorks, MATLAB, and/or ANSYS
Business	Directs team marketing and outreach, manages team budget and purchases	Strong organizational and communication skills, familiarity with web design and social media

§2.2 – Operational Cadence and Communication Flow

The team's typical weekly operational cadence is typically as depicted in Table 2.2.1. Most design tasks are initially delegated as general responsibilities to the subteam leads. It is then their role to distill the implied individual tasks, assign those to subteam members, and track that progress to ensure the broader responsibility is fulfilled. Meetings typically serve to get everyone on the same page, with more direct communication generally being conducted through Slack along with announcements made to the team or subteams.

Table 2.2.1 – Weekly Operational Cadence

Day of Week	Event/Meeting	Purpose
Monday	All-Hands Meeting	Reflect on successes and challenges of past week; Ensure unified understanding of tasks and goals for upcoming week; Maintain broad overview of current team status and timeline
Tuesday	Leads Meeting	Ensure leads and subteam leads have shared understanding of current progress on delegated responsibilities; Address any concerns and act on new challenges; Maintain active awareness of team morale and academic workloads

Wednesday-Friday	Subteam Meetings Subteam Work Sessions	Facilitate shared understanding of subteam goals by all members; Delegate tasks and follow up on individual responsibilities; Progress checkpoint comparing to goals set during All-Hands Meeting
Saturday	All-Hands Work Session	Make progress on outstanding action items, with presence of all members facilitating communication and interaction between subteams/subsystems

§2.3 – Timeline and Milestones

The team's planned and actual development timeline, along with major milestones, can be found in Fig. 2.3.1.

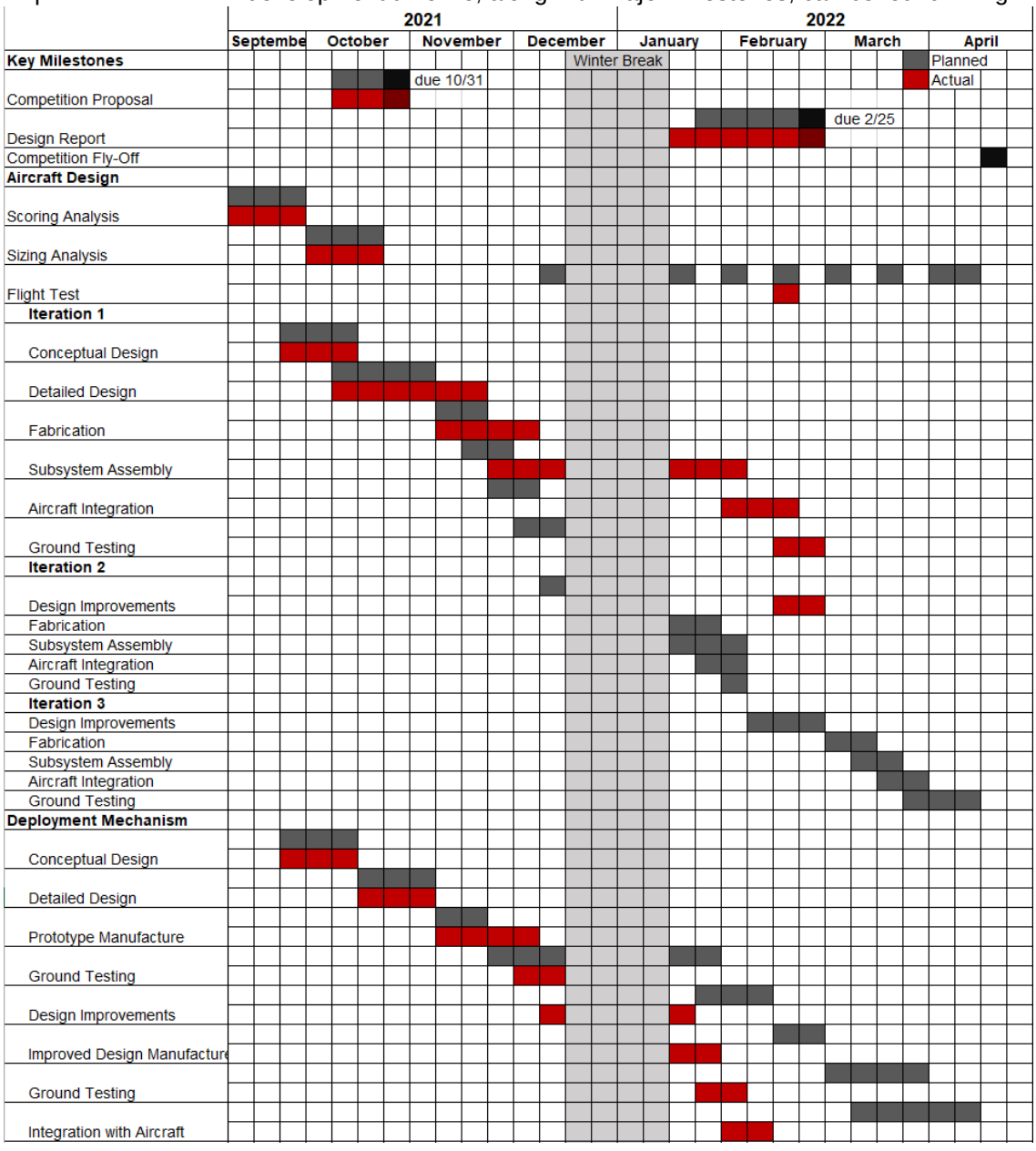

Fig. 2.3.1 – Gantt chart of planned and actual development timeline

Due to the widely unpredictable Omicron variant, progress on manufacturing and development of the aircraft was severely hindered. This impact of this was especially observed during the concluding weeks of the Fall Semester, and the January Fabrication period, which overlaps with Winter Break and was planned as a week dedicated to construction. The original deadline to complete full aircraft assembly and integration was by the beginning of

December and to have a first flight test around then as well. This was unfortunately delayed due to health concerns with coming into a public workspace for physical interaction while positivity rates rose.

§3 – Conceptual Design

§3.1 – Mission Requirements Decomposition

This section outlines the stated requirements for the four missions of the 2022 AIAA Design Build Fly Competition Fly-Off - the ground mission, and the three flight missions: the deployment flight, the staging flight, and the vaccine delivery flight. The mission specifications are organized into a list of key mission requirements that are decomposed into sets of subsystem requirements. Those subsystem requirements were used to drive configuration discussions and preliminary design decisions during the initial design phase.

§3.1.1 – Ground Mission – Operational Demonstration

In preparation of the mission, the aircraft shall be placed inside the "mission box" in the flight configuration, where the mission box is approximately 10 feet by 10 feet. The aircraft shall also contain the uninstalled maximum number of vaccine vial packages declared at Tech Inspection and the required number of syringes, which is ten times the maximum number of vaccine vial packages. The assembly crew member (ACM) and pilot shall participate in this mission and shall both start behind the start/finish line. The ACM shall be the only member to handle the aircraft and payloads. Mission timing shall begin once the ground mission official says "GO." The ACM shall load the full M2 payload then run back. Once they cross the start/finish line, timing shall stop. The mission official shall restart timing once they say "GO," where the ACM shall return to the mission box and remove the M2 payload. Once they remove the payload, they shall install the M3 payload then run back, where timing shall stop once again when they cross the start/finish line. Finally, the team shall remotely deploy the M3 payloads separately, where the Ground crew shall retrieve each and return it to the mission official. All payloads shall be deployed for the mission to count and to obtain a score. Scoring for this mission is described in Equation 1.

$$\boldsymbol{GM} = \left[\frac{Min_{time}}{N_{time}}\right] \tag{1}$$

where Min_{time} is the fastest time for all teams.

§3.1.2 – Mission 1 – Deployment Flight

The mission timing shall begin once the aircraft throttle is advanced for the first in order to take-off. No payload shall be carried by the aircraft for this mission. The aircraft shall take off and land within twenty-five feet. The mission requires the aircraft to complete three laps within a five-minute flight window. A lap shall be considered complete once the aircraft passes over the start/finish line in the air. The aircraft shall complete a successful landing to obtain a score; the landing itself is not counted as part of the flight window. Scoring for this mission is as follows for successful completion as described in Equation 2.

$$M_1 = 1.0 \tag{2}$$

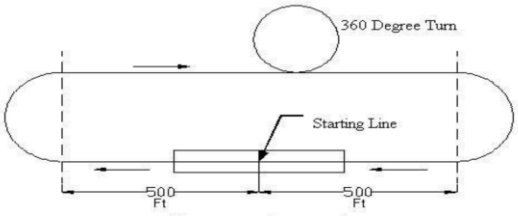

Figure 3-1: Flight Path for each Lap

§3.1.3 – Mission 2 – Staging Flight

The timing for the mission starts when the aircraft throttle is advanced for the first take-off attempt, of which the take-off length limit is 25 feet. There is a five-minute window in which the aircraft must successfully make three laps, and once this is completed, the time shall stop. To receive a score, the aircraft must land. Additionally, there must be a payload of at least ten syringes. The score for Mission 2 is a function of the number of syringes over flight time where $N_{\#\text{syringes/time}}$ is the team's score, and $Max_{\#\text{syringes/time}}$ is the highest syringes over time among all the competitors. Scoring for this mission is as described in Equation 3.

$$M_2 = 1 + \frac{N_{\#syringes/time}}{Max_{\#syringes/time}} \tag{3}$$

§3.1.4 – Mission 3 – Vaccine Delivery Flight

The timing for the mission starts when the aircraft throttle is advanced for the first take-off attempt, having a length of 25 feet. The aircraft shall fly the standard mission profile for each lap and may land anywhere on the runway and taxi to the designated vaccine vial package drop area, located on the runway 25 feet prior the Start/Finish line, following the downwind to final turn of the mission profile. The aircraft must taxi to a designated vial package drop area. The mission is complete after the final vial package is deployed and the aircraft has crossed the start/finish line, or the flight time window expires. Scoring for this mission is as described in Equation 4.

$$M_3 = 2 + \frac{N_{\#successful\ deployments}}{Max_{\#successful\ deployments}} \tag{4}$$

Table 3.1 - System Level Requirements

Req #	Requirement	References
SYS 1	The aircraft shall hold and deploy the full M2 payload of 36 syringes.	AIAA 2021-2022 DBF Rules [1] [1]
SYS 2	The aircraft shall hold and deploy the full M3 payload of three packages.	AIAA 2021-2022 DBF Rules
SYS 3	Aircraft shall take off within 25 feet.	AIAA 2021-2022 DBF Rules
SYS 4	Aircraft shall stop moving within 25 feet after mission completion.	AIAA 2021-2022 DBF Rules
SYS 5	The aircraft shall complete three (3) laps within a five-minute window.	AIAA 2021-2022 DBF Rules
SYS 6	Deploy max vaccine packages within a ten-minute window.	AIAA 2021-2022 DBF Rules

Table 3.2 - Subsystem Level Requirements

Req #	Requirement	Traceability
Mechanical Structures (MECH) Requirements		
MECH 1	The landing gear shall turn at least 10 degrees in either direction.	SYS 3, SYS 4
MECH 2	The aircraft shall move freely along the ground.	SYS 3, SYS 4
MECH 3	The fuselage shall hold at least 12 syringes.	SYS 1, SYS 2
MECH 4	The cargo space of shall be maximized to a width of 0.127 m and a height of 0.110 m.	SYS 1, SYS 2
MECH 5	The fuselage shall have door or hatch required for easy payload accessibility.	SYS 1, SYS 2, SYS 5
MECH 6	The fuselage shall dispense a minimum of one vaccine vial package.	SYS 6
MECH 7	The payload shall dispense the packages within 3.5 in – 4.5 in from the ground, avoiding the shock sensors to set off.	SYS 6
Aerodynamics and Controls (AERO) Requirements		
AERO 1	The wings shall be able to withstand the aircraft's empty mass of 3.77 kg and total masses for mission 1 and 2 of 4.62 kg and 4.43 kg.	SYS 1, SYS 2, SYS 3, SYS 4, SYS 5, SYS 6
AERO 2	The wings shall withstand a maximum deflection of 70 mm.	SYS 5, SYS 6
AERO 3	Each control surface shall deflect properly.	SYS 5, SYS 6
Propulsion (PROP) Requirements		
PROP 1	The aircraft shall be fitted with the LiPo battery operated propulsion system with less than 100 Wh of stored energy.	SYS 5, SYS 6
PROP 2	The motors and propellers shall provide a minimum total thrust of 30N.	SYS 3, SYS 5
PROP 3	The motors mount integration system shall withstand motor forces.	SYS 3, SYS 4, SYS 5
PROP 4	The aircraft propulsion mass shall not exceed 50% of the total aircraft mass.	SYS 3, SYS 4, SYS 5

§3.1.5 – Scoring

The scoring for the competition is the product of the mission score multiplied by the written report score as outlined in Equation 5. Included in the mission score are individual scores for the three missions and the ground mission as portrayed in Equation 6.

$$Mission\ Score\ =\ M_1 + M_2 + M_3 + GM \tag{5}$$

$$Competition\ Score\ =\ Mission\ Score\ \times\ Written\ Report\ Score \tag{6}$$

§3.2 – Design Parameters Sensitivity Analysis

The key characteristics of the competition aircraft were analyzed based on how they would affect the mission score. Based on the scoring equations for each mission (Equations 3.1-5), the number of syringes the aircraft carried, the aircraft's speed, and the accessibility of the aircraft's cargo were significant factors. The aircraft's potential performance was parameterized into the number of syringes it carried, Mission 2 lap time, ground mission completion time, and number of Mission 3 laps, which were based on both the velocity and cargo of the aircraft, as shown in Figure 3-2 below.

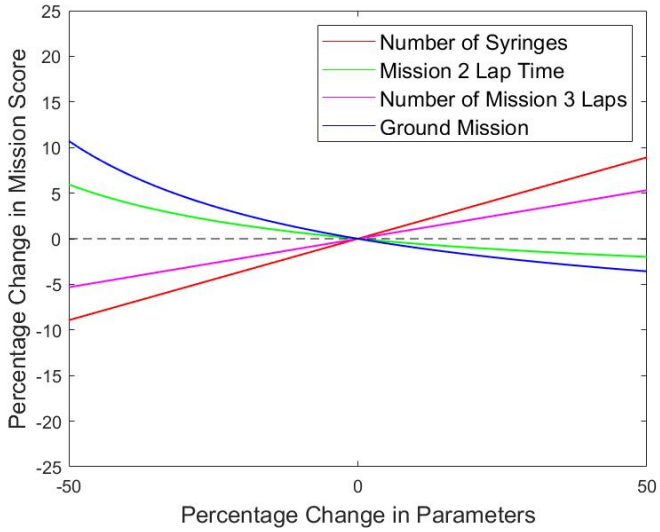

Figure 3.2.1 - Sensitivity Analysis of Mission Score to Design Parameters

Based on the results of the sensitivity analysis, the number of syringes possible for the aircraft to carry and the aircraft's thrust were maximized, but the former was prioritized since the mission score is more sensitive to the number of syringes than it is to the aircraft's speed. The accessibility of the cargo inside the aircraft by the crew was given special importance since the ground mission time would have a significant impact on the overall mission score.

§3.3 – Configuration Determination

To determine the configurations for the components of the aircraft, the team conducted an in-depth trade study to analyze the diverse options available. Using aerodynamic knowledge and information determined from previous competitions, the team narrowed down these configurations to construct the plane.

§3.3.1 – Wing Configuration

Wing placement was critical to the function of the aircraft. The team used knowledge gained from past aircraft construction along with information from Sadraey's *Aircraft Design: A System's Engineering Approach* [2] and Raymer's *Aircraft Design: A Conceptual Approach* (Raymer, Aircraft Design: A Conceptual Approach, 2018) [3]. A mid-wing configuration was rejected due to the difficult integration with the fuselage despite the benefits of low interference drag. Additionally, while a low-wing configuration would increase the aircraft's maneuverability due to increased ground effect the aircraft, it was rejected due to low stability and integration difficulty with wing-mounted motor spars. This configuration is also more prone to stalls and requires higher take-off and landing speeds, further discounting it as a possible choice. This led the team to choose a high wing for the aircraft. While this configuration is less pilot-responsive and leads to lower cruise speeds than its counterparts, the increased stability, easy fuselage integration, and low stall speeds meant it was the best choice for the team's aircraft. It also supports large wing-mounted propellers that proved to be necessary.

Wing geometry was largely dictated by manufacturability. While the low drag and high aerodynamic efficiency of an elliptical wing would benefit the aircraft, the extreme challenge of applying MonoKote to ensure an aerodynamic wing surface made an elliptical wing an impractical choice. The stall issues associated with this geometry also make

manufacturing this wing unrewarding. Similarly, a swept wing was rejected due to difficulty during construction and integration with the fuselage associated with angled wing spars. Thus, the team decided on a tapered wing to balance manufacturing challenge and aerodynamic performance. When comparing taper ratios, the team's plane is closer to a straight wing (higher ratio) to get the drag reductions of a tapered wing while still being easy to manufacture.

When determining wing geometry, both dihedral and anhedral wings were considered. While dihedral wings would increase roll stability and allow for more ground clearance, the team determined that these benefits would not outweigh the extra mass in support structure required. Similarly, anhedral wings were rejected due to the significant weight increase from support structures decreased stability and control despite the benefits of lowering the center of gravity when combined with a high wing. The team thus decided to align the wings perpendicular to the aircraft due to the potential issues associated with angled geometries.

More extreme wing configurations were considered as well. To generate more lift, the team considered using a biplane design. While this would have been useful, the extra wing also creates more drag and would have made the plane significantly heavier, especially when adding required supports between the wings. Biplanes are often notably slower as well. A tandem wing design was rejected for similar reasons. While the second wing would generate more lift, the additional weight makes the benefits unproductive. Additionally, a previous aircraft developed by the team in past years revealed that tandem wings have copious control and stability issues at this scale. The team also considered canards. This would have reduced drag caused by the tail and allowed the plane to generate more lift while also increasing maneuverability. It is, however, highly unstable and makes entering stalls risky, and this was deemed to be too big of an issue. Theoretically, the stability issues could be mitigated with a sophisticated electronic control system, but since high maneuverability would not be useful for our purposes the canard configuration was eventually rejected. Finally, a flying wing configuration was examined. This design has no definite fuselage and would allow the Mission 2 and 3 payloads to be stored across the entire body of the aircraft. This design is also relatively easy to manufacture and is an overall lighter design than many other wing configurations. Incorporating a dropping mechanism for Mission 3 would have been a challenge, however. Altogether, the team determined that the competition goals made this design unfeasible.

The team also considered different types of flaps. The overall goal was to reduce the takeoff and landing distance of the aircraft while also reducing the stall speed. While slotted flaps would have generated more lift, plain flaps were chosen because of their simplicity and ease of manufacturing.

These choices resulted in a net increase in lift force, an easier assembly, and a more reliable wing model designed to complete the necessary tasks during the missions. These decisions are highlighted in Table 3.3.1.1, with scores between one and five dictating the option's aerodynamic performance, its ease of manufacturing and integration with the aircraft.

Table 3.3.1.1 Wing Trade Matrix

Parameter	Options	Aerodynamic Score	Manufacturing and Integration Score	Total Score
Wing Configuration	**High Wing**	**3**	**5**	**8**

	Mid Wing	3	2	5
	Low Wing	4	3	7
	Biplane	3	2	5
	Tandem	2	2	4
	Canards	3	2	5
	Flying Wing	4	1	5
Wing Geometry	**High Taper Ratio**	**3**	**5**	**8**
	Low Taper Ratio	3	4	7
	Elliptical	4	1	5
	Swept	3	3	6
Wing Angle	Dihedral	4	2	6
	Anhedral	1	2	3
	No Angle	3	5	8
Flaps	Plain	4	4	8
	Slotted	5	2	7

§3.3.2 – Empennage Configuration

The Conventional, T-Tail, and V-Tail configurations were considered for the aircraft. The Conventional tail is the easiest to manufacture. It is also the most common tail type used in aviation, so it has a strong precedent for reliability. This configuration does not perform well in the event of a spin, however, and adding mechanisms to improve this would add significant weight. Additionally, wing mounted propellers create significant maneuverability issues with the elevators of a Convention tail design.

The T-Tail alleviates many of the issues with the Conventional tail. It reduces the effect of propwash on the elevators and leads to significantly greater control in spins because the airflow to the rudder is not blocked. Additionally, this design would enable greater ground clearance at the rear of the aircraft for Mission 3 deployment. These improvements come at the cost of weight, however, and the benefits provided for vaccine release did not prove necessary for our mechanism.

Similarly, the V-Tail resolves many of the problems that the Conventional tail creates while also improving on issues with the T-Tail. It is a much lighter configuration due to the smaller surface area and material requirement. This also reduces the overall drag produced by the tail. Additionally, this configuration leads to less propwash on the vertical stabilizer that could cause damage. This option is far more complex than either of the other configurations considered, however, because the elevators and the rudder need to be combined. This makes designing control surfaces for turning or pitching difficult. If our aircraft had major propwash issues, this tail would be a great option.

While the V-Tail and T-Tail configurations offer several improvements over the Conventional tail, the tradeoffs are too great. The Conventional tail was chosen due to its ease of manufacture, reliability, and limited weaknesses

compared to other options. These decisions are highlighted in Table 3.3.2.1 using the same scoring scheme as Table 3.3.1.1.

Table 3.3.2.1 Empennage Trade Matrix

Parameter	Options	Aerodynamic Score	Manufacturing and Integration Score	Total Score
Tail Geometry	**Conventional Tail**	**3**	**5**	**8**
	T-Tail	4	2	6
	V-Tail	5	1	6

§3.3.3 – Propulsion Configuration

Multiple propulsion configurations were considered based on preliminary scoring analysis' predicted payloads. Using eCalc, an online R.C. aircraft performance calculator, the team tested different motor arrangements. Initially, the team considered implementing the pusher-style configuration instead of the standard tractor-style system. While this would have allowed for more clearance during taxi missions, it requires a challenging mounting setup and could cause airflow disruptions. From here, research made it clear that a single motor would be unable to lift the size of aircraft the team needed to build. Configurations with multiple motors were challenging because of the competition's power limit and were costly. This led the team to settle with a wing-mounted two motor setup.

Different propeller configurations were considered as well. While a small propeller allowed for easy integration with the Mission 3 dropping mechanism, the thrust proved to be too small to carry the expected payload. Additionally, the high-wing configuration combined with wing-mounted motors reduced the potential problems caused by the large propeller. From this analysis, the team decided to incorporate two, larger-sized propellers with our aircraft.

Propellers with various pitches were analyzed. While the low drag of small pitch configurations would be beneficial, they proved to produce too little thrust to be viable. The larger drag was deemed to be an acceptable tradeoff for higher thrust with a large, high pitch propeller. These propellers also increase pitch speeds and help the aircraft reach the desired cruise speed at heavier weights.

Design decisions in Tables 3.3.3.1, 3.3.3.2, and 3.3.3.3, below highlight how propulsion systems were scored to determine a configuration that creates sufficient thrust with the easiest integration.

Table 3.3.3.1 Motor Configuration Trade Matrix

Parameter	Options	Thrust Score	Power Score	Cost Score	Total Score
Motor Configuration	1 Motor	1	3	4	8
	2 Motors	**4**	**2**	**3**	**9**
	3 Motors	5	1	2	8

Table 3.3.3.2 Propeller Size Trade Matrix

Parameter	Options	Thrust Score	Integration Score	Total Score
Propeller Size	Small	1	5	6
	Large	**5**	**3**	**8**

Table 3.3.3.3 Propeller Pitch Trade Matrix

Parameter	Options	Thrust Score	Drag Score	Total Score
Propeller Pitch	**High Pitch**	**5**	**3**	**8**
	Low Pitch	2	5	7

§3.3.4 – Fuselage Configuration

The shape of fuselage was important in preparing our aircraft for Mission 2 and 3 and was therefore designed with these payloads in mind.

The rectangular prism shape of the vaccine vial packages combined with the near-rectangular profile of an array of syringes meant that a round fuselage would have proven difficult in future design. Additionally, a circular cross section of the fuselage would result in having empty volume within the fuselage as the cross section of the payloads are mostly rectangular. For these reasons, cylindrical fuselages were rejected.

Several fuselage construction configurations were analyzed. A truss structure was considered because of its overall strength. The internal triangles make this design able to withstand strong compressive and tensile forces. This strength comes at the expense of weight however, and the truss structure was deemed to be too heavy for the team's aircraft. When considering lighter options, a monocoque shell fuselage was examined. With external skin providing the main structure, this design would be lightweight and aerodynamic. Despite this, the design was rejected due to its lack of strength and difficulty to manufacture. Issues with a truss design and a monocoque shell design led the team to choose a semi-monocoque shell design. Stringers in between ribs increase the strength of basic monocoque design while remaining light. This design also allows MonoKote to be easily integrated with the aircraft, helping to keep the structure aerodynamic.

These decisions led the aircraft's fuselage to be light while supporting the payloads required for Missions 2 and 3. These decisions are summarized in Table 3.3.4.1 with a similar scoring scheme to the matrices above.

Table 3.3.4.1 Fuselage Trade Matrix

Parameter	Options	Strength Score	Manufacturing Score	Total Score
Fuselage Construction	Truss	4	2	6
	Monocoque Shell	1	3	4
	Semi-monocoque Shell	**3**	**4**	**7**

§3.3.5 – Landing Gear Configuration

Two landing gear configurations were considered for the aircraft. Firstly, the team analyzed a tail-dragger system. This arrangement generates less drag and is lighter overall. Despite this, it is more difficult to taxi in high winds, and steering is generally more challenging because it is guided by the rear wheel. While the tricycle configuration is heavier and generates more drag, it provides better maneuverability on the ground. Given the number of takeoffs and landings required for this year's competition, the team decided that a tricycle system would be the best option for our aircraft.

After determining the landing gear configuration, the team considered whether to use wheels or skis. Both offer strong advantages for specific performance capabilities, and each could be viable for the aircraft. Wheels provide the aircraft with greater steering capabilities and easier control overall, but struggle when they encounter uneven terrain. Skis, while they will not fall into cracks in the runway, still struggle with rough terrain and generate a lot of

friction. The additional challenge of steering a ski landing gear made using wheels a superior option for our aircraft. The team also considered retractable landing gear. While this would reduce drag in the air, this configuration is ineffective for Missions 2 and 3 because of the loss of important fuselage space to accommodate the mechanisms. Furthermore, this would add a significant amount of weight, making it unfit for the team's aircraft.

The chosen landing gear configuration makes the team's aircraft maneuverable and resistant to forces from frequent take-offs and landings. The decisions made during this preliminary design are displayed in Table 3.3.5.1 with a similar scoring scheme to the above matrices.

Table 3.3.5.1 Landing Gear Trade Matrix

Parameter	Options	Ground Score	Air Score	Total Score
Gear Configuration	**Tricycle**	**5**	**3**	**8**
	Tail Dragger	2	4	7
Landing Options	**Wheels**	**4**	**5**	**9**
	Skis	3	5	8

§4 – Preliminary Design

§4.1 – Design and Analysis Methodology

The team has modified its design and analysis process to echo the systems engineering approach used in spacecraft design. The entire development process, from the design phase and build phase to the flight phase, is charted in Figure 4.1.1.

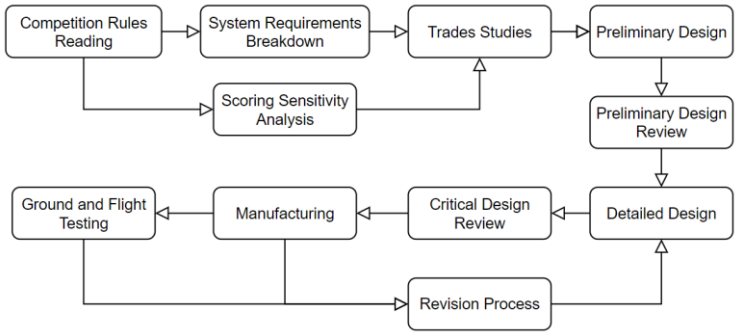

Fig. 4.1.1 Team Design and Analysis Methodology

The competition rules provide information to conduct a scoring sensitivity analysis, which suggests the relative importance of each mission on the team score and recommends a set of aircraft performance parameters to optimize for. The competition rules are also organized into a set of mission requirements of the aircraft. These mission requirements are further broken down into subsystem requirements for the aircraft, providing a critical list of quantitative performance parameters that the aircraft is verified and validated against in the ground and flight-testing phase of the overall aircraft development process. This ensures that the aircraft both meets design expectations and fulfills the competition specifications for each mission. The subsystem requirements are then conceptualized in a set of trade studies that analyze a broad range of design options and score them for a set of

criteria. Trades scoring criteria vary from the effectiveness of the design option to fulfill a subsystem requirement to the ease of design and manufacturing based on the capabilities of the team. The key takeaway from the trades studies is a determination of the overall aircraft geometry and configuration, an idea of what the aircraft shall look like.

The preliminary design process elaborates upon the conclusions of the trade studies to determine a set of essential aircraft design parameters that may be used in the detailed design. For example, the team elaborates on the wing in the preliminary design phase by taking the large wingspan recommended by the scoring analysis, the recommended high wing configuration from the trade studies, and the related mission and subsystem requirements to determine factors such as the wingspan, taper ratio, airfoil and control surface size. The team gathers for a preliminary design review for a sanity check that the overall design parameters are sound and do not conflict with competition rules before the detailed design process begins.

The detailed design process uses the design parameters to develop the aircraft in complete detail. For example, the wing design parameters and the mass budgeted for the aircraft wing are used to create a computer aided design (CAD) model of the airfoil ribs and stringers that shall make up the wings semi-monocoque structure. The critical design review is conducted to analyze each component of the aircraft against the subsystem requirements it fulfills and performs a final check of all the design details prior to any manufacturing begins. This has significantly facilitated the team's progress this year and has caught mistakes that would have cost a considerable amount of time and expenditure to fix during the build phase.

The manufacturing process follows the critical design review, and a list of revisions is created at this point in the development process to record all manufacturing difficulties and problems discovered during ground and flight testing. These revision results are analyzed after the testing process, alongside the testing results that are compared against the system requirements for proper verification and validation. Any corrections that need to be made in the revision process are then added iteratively, per each test cycle, to the detailed design of the aircraft.

§4.2 – Design and Sizing Trade Studies

§4.2.1 – Aircraft Sizing

The aircraft is sized based on the results of the sensitivity analysis and the conceptual trade studies. Whereas the trade study mentioned in Section 3 determines the overall configuration of the aircraft, the trade studies that follow in Section 4 are more detailed and either provide quantitative parameters for the detailed design to use or determine components to be purchased that fulfill the subsystem requirements.

The sensitivity analysis results highlight the importance of maximizing aircraft mass by designing for a large wingspan and maximizing thrust. Thrust was maximized assuming constant power expenditure of the maximum allowable battery capacity through the maximum flight time of Mission 3, to be elaborated upon in Section 4.2.2. The aircraft total mass was predicted using two methods based on the constant power expenditure. The first, assumes perfect conversion of electrical power into mechanical power, and calculates the mass of the aircraft given the general trend of specific power amongst RC planes. For a slower flying RC aircraft, the specific power is expected to be in the range of 150 to $200\ \mathrm{W kg^{-1}}$. For a constant $600\ \mathrm{W}$ power expenditure, this results in an expected range of 2.5 to $4\ \mathrm{kg}$ for total aircraft mass. The second method is based upon the expected stall thrust of

the aircraft, described in greater detail in Section 4.2.2. Assuming a total maximum thrust of 30 N, we may expect a healthy thrust to weight ratio (TWR) of 0.8 for a slow flying aircraft, which recommends a mass of $3.7\ \mathrm{kg}$. The range of predicted mass is used as an initial mass in the aircraft sizing process.

The team initially selected the MH114 airfoil as the wing's primary airfoil because it had been previously used by the team in previous years. Using predicted values of RC aircraft airspeed and initial values of aspect ratio and taper ratio, the team generated an expected range of Reynold's numbers that the aircraft is predicted to operate in. The Reynolds number was on order of $\mathrm{Re} = 10^5$. Using data from airfoiltools.com [4] [5] on the MH114 airfoil operating between $1 \times 10^5 < \mathrm{Re} < 5 \times 10^5$, we determined an infinite-wing lift curve slope of $c_{L_\alpha} = 6.11$. The non-ideal, sub-2π value is attributed to the simple drag and turbulence modeling present in XFoil. For a rectangular tapered wing with zero wing sweep, we use Equation 7 to determine the Oswald span efficiency (our analysis assumes a quadratic trend for form drag) [6].

$$e = 1.78(1 - 0.045AR^{0.68}) - 0.64 \tag{7}$$

The finite-wing coefficient of lift C_{L_α} is determined using Equation 8.

$$C_{L_\alpha} = \frac{c_{l_\alpha}}{1 + \frac{c_{l_\alpha}}{\pi e AR}} \tag{8}$$

The maximum coefficient of lift $C_{L_{\max}}$ is obtained by approximating the stall angle with respect to zero lift axis as the same as that of the infinite wing, as seen in Equation 9.

$$C_{L_{\max}} = C_{L_\alpha} \bar{\alpha}_{\max} \tag{9}$$

Using the maximum wingspan b specified by requirements, the aspect ratio AR and the taper ratio λ, we obtain the root chord c_r geometrically to determine the wing surface area S (taken to be the characteristic surface area of the whole aircraft) using Equation 10. The taper ratio is a tuning factor chosen to be a value to ensure that a carbon fiber spar can fit through the wingtip. The aspect ratio is a tuning factor that is varied to achieve acceptable performance in terms of aircraft speed and takeoff length.

$$S = \frac{b}{2} c_r (1 + \lambda) \tag{10}$$

To evaluate whether the chosen wing parameters are appropriate for the aircraft, we compare the wing loading $\frac{mg}{S}$ to expected values for RC aircraft. The wing loading is evaluated to be $6.6\ \mathrm{kgm^{-2}}$, which is in the normal range for RC aircraft which vary from $5\ \mathrm{kgm^{-2}} < \frac{mg}{S} < 10\ \mathrm{kgm^{-2}}$. A low wing loading helps with shortening the takeoff distance. One of the primary challenges of the competition is to ensure a heavy RC aircraft may takeoff on a 25 ft runway. To calculate the takeoff distance, we first calculate the aircraft stall speed using Equation 11.

$$V_s = \sqrt{\frac{mg}{S} \frac{2}{\rho C_{L_{\max}}}} \tag{11}$$

Expecting takeoff to safely occur at takeoff speed $V_{TO} = 1.3V_s$, we approximate the takeoff acceleration as that evaluated at 70% of the takeoff speed, as shown in Equation 12.

$$\Gamma_{07} = \frac{F}{m} - \frac{\frac{1}{2}\rho V_{TO}^2}{m}\left(C_{Dg} - fC_{Lg}\right) - gf \tag{12}$$

The acceleration is calculated using the ground drag and lift coefficients, C_{Dg} and C_{Lg}, evaluated at 0 angle of attack, and a dry runway friction of $f = 0.03$. The kinematic Equation 13 calculates the runway length.

$$L_r = \frac{1}{2}\frac{V_{TO}^2}{\Gamma_{07}} \tag{13}$$

The cruise calculation is performed with maximum thrust, as minimization of drag is not an important consideration per the subsystem requirements. The maximum speed is solved using the coefficient of drag at zero lift C_{D_0} obtained from airfoiltools.com for the airfoil and the calculated parameters above, using Equation 14. We expect the aircraft to be able to complete the mission at maximum speed within the time constraints.

$$F = \frac{1}{2}\rho V^2 S C_{D_0} + \frac{1}{\pi e A R}\frac{2m^2 g^2}{\rho V^2 S} \tag{14}$$

This sizing process occurs repeatedly to evaluate a set of input dimensions for the wing and ensure that the design meets the subsystem requirements. Of the constraints provided by the requirements, the short takeoff and landing runway length is far more restrictive than the flight time constraints. The goal is to obtain the largest maximum takeoff weight (MTOW) for the design, which allows for more payload to be carried. Figure 4.2.1.1 describes the process graphically.

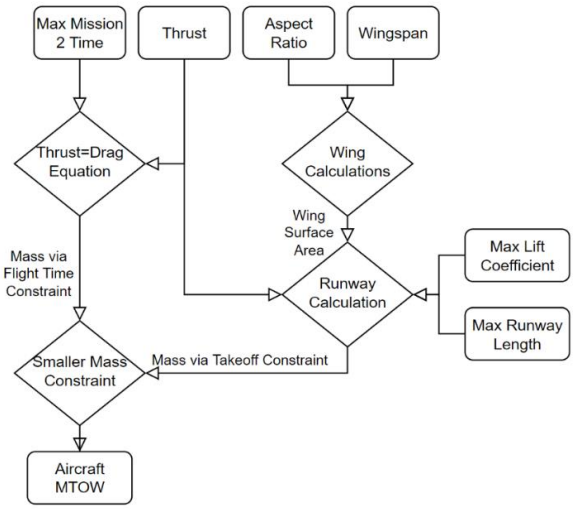

Fig. 4.2.1.1 Sizing Analysis Flowchart

The flight time calculations are provided in Section 4.4 for mission performance, and the initial quantitative results for the preliminary design lift, drag and stability are also provided in Section 4.4.

§4.2.2 – Propulsion

§4.2.2.1 – Motor Configuration

For this year's competition, it is important to generate large amounts of static thrust to ensure the aircraft could quickly land and take-off numerous times in a short distance. To do this, a high motor RPM would be necessary, and thus, it was advantageous to maximize the battery voltage and choose motors designed to generate high quantities of thrust with mid-to-low Kv ratings. However, the watt-hour limit stipulated in the AIAA Design Build Fly Competition Rules limited battery capacities.

Low battery capacities, in turn, limited the aircraft flight time. With a single motor, eCalc's propCalc software predicted that the aircraft would only be able to fly for seven minutes while producing the required 30N of thrust determined by sizing analysis. To increase flight time, the propulsion team decided to divide the thrust generated between two motors. While maintaining a constant speed, the propeller diameter could be reduced, lowering the rate of power consumption from each motor. As a result, the stored energy could power the motors for longer, increasing the total available flight time. A smaller propeller diameter also lowers the design's clearance requirement between the plane and the ground, allowing for a shorter landing gear, a lower center of gravity, and greater stability upon landing.

To confirm intuitions about the trade-offs of using a single motor and a twin motor system, the team used equations derived from Model Airplane Propellers [7] and Figure 4.2.2.1.1 to graph the relationship between increasing propeller diameter and flight time available (see Figure 4.2.2.1.1.)

$$Thrust_2 = Thrust_1 \left(\frac{D_2}{D_1}\right)^4 \tag{15}$$

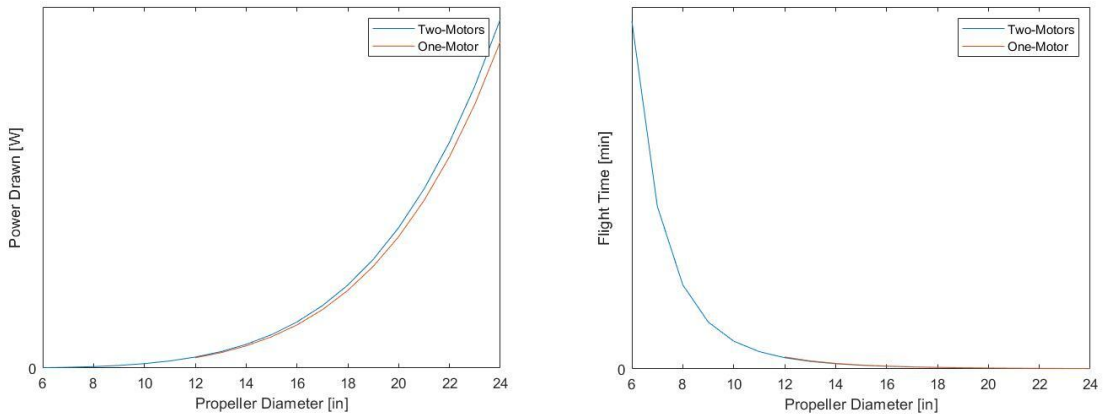

(A) (b)

Fig. 4.2.2.1.1 MATLAB plots comparing the theoretical performances of single and dual motor designs. Fig. 4.2.2.1.1a on the left plots the power drawn as a function of propeller diameter, and Fig 4.2.2.1.1b on the right plots the projected flight time as a function of propeller diameter.

Per the graphed results, as the propeller diameter increased, the power drawn by the motor increases and the total flight time decreases. This relationship holds for single and twin motor configurations, with more power drawn by twin motor systems when using larger propellers. Whereas a high minimum diameter for a single motor configuration was necessary to produce the 30N of required net thrust, to maximize flight time and minimize the rate of power draw, a smaller propeller diameter was the optimal design choice. Thus, the team chose a twin motor system.

As a result of a twin motor design, the team encounters greater propeller effects such as unintentional yaw due to angular moments. A conventional single motor system generates angular momentum at the central axis that can be counteracted by the pilot using control surfaces. A twin motor design increases the distance between the motor

and the central axis, allowing for a greater moment to act on the plane. To account for this, the team chose counter-rotating propellers to balance the moment effects.

§4.2.2.2 – Motor Selection

Modeling the competition aircraft after slow-flying cargo planes, the propulsion team determined that the ratio of power required per kilogram of mass should be similar to that of general aviation slow-flying aircraft. For low wing-loading, this ratio is typically $\frac{50W}{1\,lb} \cong \frac{110W}{1kg} = \frac{P}{m}$. The power required for each mission was then determined using Equation 16. Using this equation and the ratio of power t006F mass, the power requirements for each mission could be computed. Table 4.2.2.2.1 shows the computed power necessary for each mission.

$$P_{required} = \frac{P}{m} \times mass \tag{16}$$

Table 4.2.2.2.1 Power requirements and mass of each mission

Mission	Mass of Plane (kg)	Power Required (W)
Mission 1	3.72 kg	333 W
Mission 2	4.42 kg	487 W
Mission 3	4.38 kg	481 W

The maximum quantity for power required of the three missions constrains the design as it determines the minimum amount of power needed to fly all three missions. Using this power constraint, the team limited consideration to motors that could satisfy this requirement and fell within the target Kv range of 250-400 Kv. After analyzing some of the possible motors, the team shortlisted three potential motors (Table 4.2.2.2.2).

Table 4.2.2.2.2 Shortlisted motor specifications

Motor Name	Unit Weight	Max Power Rating	Unit Cost
Cobra CM-3520/28	0.234 kg	575 W	$63
Scorpion S-4035-250	0.45 kg	2700 W	$170
Cobra CM-4012/30	**0.141 kg**	**490 W**	**$70**

After comparing motor weight, cost, and maximum power rating, the team chose the Cobra CM-4012/30 motor for the aircraft's propulsion design. The Scorpion S-4035-250 was thoughtfully considered due to its ability to provide high thrust. However, the motor's high cost ultimately outweighed the benefit of a cheaper and lighter motor.

§4.2.2.3 – Power Plant

The competition restrictions dictate a maximum of 100 Wh in total propulsion power stored in the aircraft. The team concluded that there was no reason to use any less stored power, and as a result, chose a configuration providing 99.9 Wh of stored energy. It was also advantageous for the team to provide as much voltage to the motors as possible, thus, six cell batteries connected in series, each cell storing 3.3 volts, was optimal for this year's iteration, totaling 22.2 volts of electrical potential. This stipulated that the capacity of the battery configuration needed to be 4500 mAh to achieve the 99.9 Wh of stored energy initially determined. As the team decided on a twin motor system for this year's competition, two separate battery packs are required to power each motor, thus each pack would provide a capacity of 2250 mAh. Assuming that the battery is discharged to 85%, it is estimated that only 84.9 Wh are truly available.

The propulsion team desired a motor capable of a higher RPM to generate more thrust and travel faster. According to the chosen motor's (Cobra CM-4012/30) specifications, each motor has a Kv rating of 300. Equation 17 determines that the maximum RPM for each motor is 6700 RPM. Both motors rotating at 6700 RPM generates sufficient thrust to power our aircraft.

$$Kv\,rating \times Voltage = RPM \tag{17}$$

§4.2.2.4 – Propeller Selection

To determine the propeller diameter and pitch, minimum and maximum values for power drawn during flight are required. Assuming that the aircraft is in the air for the entirety of the time allotted per mission (10 minutes), the minimum power drawn can be calculated using Equation 18. It then follows that the minimum power required is 254.7W.

$$P_{min} = \frac{E_{available}}{t} \tag{18}$$

The maximum power drawn is the maximum power required for all three missions was determined in section [Motor Selection]. Thus, the maximum power draw required is 487 W.

Using the equation for static thrust derived from the Rankine-Froude Momentum Theory [7], the required static thrust, determined by sizing, can be expressed as a function of the disc area of the propeller. Because area is a function of the radius, the following equations solve for propeller diameter in terms of power and required static thrust.

§4.2.2.5 – Parameters Used In Propeller Dimension Calculations

To perform calculations to determine the diameter of the propeller the team calculated and set certain parameters. The initial analysis required at least 30N of total static thrust, or a static thrust per motor T_{static} of 15 N. Estimating the area of sample spinners gave that $A_{spinner} = \frac{\pi}{4}\ \text{in}^2 = \frac{\pi}{6200}\ \text{m}^2$. From section 4.2.2.4, the minimum and maximum power required is 254.7 W and 487 W respectively. Using these parameters, T_{static} can be calculated using Equation 19.

$$T_{static} = .85P^{\frac{2}{3}}(2\rho A_2)^{\frac{1}{3}}\left(1 - \frac{A_{spinner}}{A_2}\right) \tag{19}$$

An upper limit on the amount of static thrust needed is required to determine the maximum propeller diameter the aircraft can have. Where sizing analysis determined the minimum required static thrust per motor was 15 N, the team set an upper limit of 25 N on each motor, so our net thrust generation at takeoff does not exceed 50 N. Substituting the minimum power drawn from one motor if the aircraft were to fly for the entire ten minutes allowed per mission, the team derived that the maximum diameter is 0.35m or 13.8 inches.

To determine the minimum possible diameter of the propeller, the team substituted maximum power draw expected from all three missions, P_{max}, and solved for the minimum value of static thrust required (15N). This yields a minimum propeller diameter of 2.8 inches.

After determining the interval over which to vary the diameter of the propeller when analyzing propulsion configurations in eCalc, the team limited the minimum and maximum values for pitch of the propeller. The general

relationship between pitch and propeller diameter expressed in Equation 20 yields a minimum and maximum propeller pitch of 1.7 inches and 11.7 inches respectively.

$$60\% \times diameter \leq Pitch \leq 85\% \times diameter \tag{20}$$

Using the calculated intervals for possible propeller diameter and pitch values, the team limited the list of possible propellers to those freely available to purchase, before analyzing possible configurations using the propCalc software from eCalc. The top configuration choices were as follows. All configurations were based on our chosen motor.

Table 4.2.2.5.1 - Selected Propeller Specifications

Option	Flight Time	Thrust at Takeoff Per Motor	Propeller Diameter	Propeller Pitch	Motor Load
Choice 1	10.7 min	19.7 N	13 in	9 in	6.34 C
Choice 2	10.1 min	18.8 N	12 in	9 in	6.44 C
Choice 3	9.6 min	19.0 N	14 in	12 in	7.3 C

Many of the possible configurations resulted in a warning in eCalc that pitch speed was too low – less than twice the stall speed. To ensure that the aircraft design was feasible, pitch speed and stall speed were computed manually to verify if the warning was correct. Using Equations 21 and 22, we can compute the pitch speed and stall speed to be $23.4\ \mathrm{ms}^{-1}$ and $6.6\ \mathrm{ms}^{-1}$ respectively. From there, Equation 23 calculates the factor of safety to be 3.5.

$$V_{Pitch} = RPM \times Pitch \tag{21}$$

$$V_{Stall} = \sqrt{\frac{2W}{S_w \rho C_L}} \tag{22}$$

$$\eta = \frac{V_{Pitch}}{V_{Stall}} \tag{23}$$

Due to eCalc using a default value of 1.0 for coefficient of lift while the team's design had a coefficient of lift of 1.8, the stall speed is lower than that calculated with eCalc. As a result, the factor of safety of 3.5 is reasonable for flight.

§4.3 – Tail Sizing

The tail sizing procedure began once the major parameters of the wing and fuselage were determined. The parameters of the tail were repeatedly tuned to achieve a static margin between 5%-15% for all three missions. The static margin was the measure evaluated to determine if the tail would make the plane more stable and less maneuverable or less stable and more maneuverable.

The tail was initially sized with the volume ratios V_H 0.7 and V_V as specified by Raymer for general aviation single engine aircraft [5]. Fig. 4.3.1.

	Typical values	
	Horizontal c_{HT}	Vertical c_{VT}
Sailplane	0.50	0.02
Homebuilt	0.50	0.04
General aviation—single engine	0.70	0.04
General aviation—twin engine	0.80	0.07
Agricultural	0.50	0.04
Twin turboprop	0.90	0.08
Flying boat	0.70	0.06
Jet trainer	0.70	0.06
Jet fighter	0.40	0.07
Military cargo/bomber	1.00	0.08
Jet transport	1.00	0.09

Fig. 1 - Tail Volume Coefficients

The total length of the aircraft to be 1.83m from nose plate to trailing edge of the tail to contribute to move the CG back. Using the Equations 24 and 25, lengths and widths of each stabilizer were dictated by their respective aspect ratios.

$$V_V = \frac{S_V * l_V}{S_w * B_w} \tag{24}$$

$$V_H = \frac{S_H * l_H}{S_w * c_w} \tag{25}$$

Aerotoolbox specifies that vertical stabilizers typically have aspect ratios between 1.3-2, an aspect ratio of 2 of chosen as the lift is prioritized more than maneuverability for our design [10]. Aerotoolbox also specifies that the aspect ratio of the horizontal stabilizer should be less than that of the wing, so an AR of 3 was chosen [10]. The Equation 26 was used to find the spans and chords of the respective stabilizers.

$$AR = \frac{b^2}{S} = \frac{2b}{c_r(1+\lambda)} \tag{26}$$

The vertical stabilizer has a span of 0.3912m and a root chord of 0.26. The horizontal stabilizer has a span of 0.716m and a chord length of 0.236m. The lengths of rudders and ailerons should be between 25%-50% of the length of the tail chord [5]. They were chosen to be 25% of the chord length to reduce mass and allow the servos to control them easily. The length of the rudder is 0.065m and the length of the elevators is 0.059m. The tail was sized first through calculations so that it could be modeled in AVL to undergo more rigorous analysis later in the design process.

§4.4 – Performance Predictions

§4.4.1 – Aircraft Performance

Many of the performance prediction methods were used in the initial sizing study of Section 4.1, to be repeated here for convenience. The aircraft's lift is calculated using data from airfoiltools.com for the selected airfoil's coefficient of lift and drag as a function of angle of attack. Because the XFOIL analysis on airfoiltools.com [4] incorporates basic drag and turbulence modeling, we obtain an infinite wing lift curve slope c_{L_α} that is less than the ideal 2π expected from potential flow and thin airfoil theory. The aspect ratio AR, taper ratio λ, wingspan b are used to calculate the wing surface area (planform area) S through root chord c_r in Equation 10 as repeated here as Equation 27.

$$S = \frac{b}{2} c_r(1+\lambda) \tag{27}$$

The finite-wing lift curve slope is calculated using Oswald efficiency from Equation 7, repeated here as 28, and Equation 8 [6], repeated here as Equation 28.

$$e = 1.78(1 - 0.045AR^{0.68}) - 0.64 \tag{28}$$

$$C_{L_\alpha} = \frac{c_{l_\alpha}}{1 + \frac{c_{l_\alpha}}{\pi e AR}} \tag{29}$$

The maximum coefficient of lift $C_{L_{\max}}$ is obtained by approximating the stall angle with respect to zero lift axis as the same as that of the infinite wing, as seen in Equation 9, now repeated here as 30.

$$C_{L_{\max}} = C_{L_\alpha}\bar{\alpha}_{\max} \tag{30}$$

The drag assumes a quadratic trend for form drag (by use of the Oswald efficiency) and is calculated using Equation 31. Equation 31 is a combination of the drag equation and has the lift coefficient substituted with a constraint from setting the lift to equal the aircraft weight. The coefficient of drag with respect to zero lift is obtained from data in airfoiltools.com.

$$D = \frac{1}{2}\rho V^2 S C_{D_0} + \frac{1}{\pi e AR}\frac{2m^2 g^2}{\rho V^2 S} \tag{31}$$

The lift coefficient is evaluated at an expected 10 degrees angle of attack for the rotation after achieving takeoff speed V_{TO}. The cruise lift and drag coefficients are evaluated under the condition that the drag equals the maximum thrust of the aircraft. The takeoff thrust is taken from the propulsion trade study, the runway length is calculated per Section 4.1 methods and the maximum crosswind capability for landing is calculate using a maximum bank angle of 10 degrees and the takeoff lift coefficient for Equation L14.

$$V_w = -\frac{\phi}{C_{y_\beta}}\sqrt{\frac{2mgC_L}{\rho S}} \tag{32}$$

lift coefficient is evaluated at an expected 10 degrees angle of attack for the rotation after achieving takeoff speed V_{TO}. The cruise lift and drag coefficients are evaluated under the condition that the drag equals the maximum thrust of the aircraft. The takeoff thrust is taken from the propulsion trade study, the runway length is calculated per Section 4.1 methods and the maximum crosswind capability for landing is calculate using a maximum bank angle of 10 degrees and the takeoff lift coefficient for Equation L14.

The full list of performances is displayed in Table 4.4.1.1 for the maximum takeoff weight (MTOW) and empty weight. The very basic drag modeling of the aircraft does not consider fuselage effects and therefore severely underestimates the aircraft's drag properties, which results in an excessively high cruise speed.

Table 4.4.1.1 List of Preliminary Design Performance

Variable	Meaning	Performance, empty (M1)	Performance, MTOW (M2, M3)
m	Total Aircraft Weight	2.75 kg	4.5 kg
$C_{L_{\max}}$	Maximum Lift Coefficient	1.52	
V_s	Stall Speed	5.84 ms^{-1}	7.5 ms^{-1}
V_{TO}	Takeoff Speed	7.59 ms^{-1}	9.7 ms^{-1}
V_c	Cruise Speed (Maximum Speed)	29 ms^{-1}	29 ms^{-1}
C_{L_g}	Takeoff Lift Coefficient	1.36	0.90
-	Takeoff Lift Force (at 10 degrees AoA)	40.7 N	66.8 N
C_{D_g}	Takeoff Drag Coefficient	0.19	0.13
-	Takeoff Drag Force (at 10 degrees AoA)	5.7 N	9.3 N
C_{L_c}	Cruise Lift Coefficient (Lift Coefficient at Max Thrust)	0.06	0.10
-	Cruise Lift Force	27.0 N	44.2 N

C_{D_c}	Cruise Drag Coefficient (Lift Coefficient at Max Thrust)	0.09	0.09
-	Cruise Drag Force	39.5 N	40 N
L_r	Takeoff Runway Length	2.37 m	7.17 m
-	Maximum Crosswind Capability	5.43 ms^{-1}	6.95 ms^{-1}
F	Takeoff Thrust	39.4 N	
TWR	Thrust to Weight Ratio	1.46	0.89
Re	Operating Range of Reynold's Numbers	$1.8 \times 10^5 < Re < 6.9 \times 10^5$	

§4.4.2 – Aircraft Stability

To understand the stability characteristics of the aircraft and determine a range of acceptable CG positions for an adequate 5% to 15% static margin, the team used Athena Vortex Lattice (AVL) software developed by Professor Mark Drela at Massachusetts Institute of Technology [8]. The aircraft's maximum mass, as calculated by the sizing process, was used as an input along with the wing and tail geometric parameters to create a simple model of the aircraft's stability characteristics. A basic analysis was performed using historical team trends of aircraft surface mass density in order to determine an approximate inertia matrix for the aircraft. Specifically, previous team aircraft were analyzed for the mass of their wing and tail surfaces and surface densities were calculated assuming a constant density throughout the surface. The CG is placed in the AVL analysis in order to achieve the static margin based on AVL's calculation of the aircraft's neutral point. The AVL results are displayed in Table 4.4.2.1 and represent the stability derivatives with the maximum takeoff weight.

Table 4.4.2.1 List of Preliminary Design Stability Derivatives

Stability Derivative	Meaning	Value
C_{L_α}	Lift force due to angle of attack (lift curve slope)	4.585
C_{m_α}	Pitch moment due to angle of attack (function of static margin)	-0.767
C_{y_β}	Lateral force due to sideslip (yaw damping)	-0.270
C_{l_β}	Roll moment due to sideslip (dihedral effect, spiral stability)	-0.090
C_{n_β}	Yaw Moment due to sideslip (route stability effect, yaw feedback)	0.179
C_{y_p}	Lateral force due to roll velocity	0.290
C_{l_p}	Roll moment due to roll velocity (roll mode damping)	-0.441
C_{n_p}	Yaw moment due to roll velocity	-0.135
C_{y_r}	Lateral force due to yaw velocity	0.293
C_{l_r}	Roll moment due to yaw velocity (yaw/roll coupling)	0.331
C_{n_r}	Yaw moment due to yaw velocity (yaw damping)	-0.233

The results in Table L2 are reassuring to the team, as all the stability derivatives (excluding lift curve slope of course) are in order of unity and in the expected positive or negative values. The results serve as confirmation that our conventional airplane design shall perform as a conventional aircraft would. The AVL results also confirm some of the calculations made in the initial stages of preliminary design, since the C_{L_α} value obtained from AVL is the same (± 0.005) as the value obtained through hand calculations.

The static margin is calculated to be at 15.4%, but this is taken as a very rough approximation as the final aircraft mass and inertia will be different due to the crude mass approximations made. The team is also unable to anticipate the mass and inertia contributions of the adhesives and surface coating of the aerodynamic surfaces, which contributes to the uncertainty of the values shown. Notably, an area of concern for the team is that the spiral stability criterion shown as Equation L14 is evaluated very low at a value of 0.355, and warrants flight testing to confirm airworthiness.

$$\frac{C_{l_\beta} C_{n_r}}{C_{l_r} C_{n_\beta}} = 1 \tag{33}$$

The stability results were only generated for a single configuration with maximum takeoff weight because the mass and inertia approximations produce uncertainties that would make any differences between the stability of each configuration nonsensical and largely due to approximation error.

§4.4.3 – Mission Performance

To calculate the completion times for each mission, we consider the time taken to complete one lap. The time taken in straight and level flight for the straight leg of the lap is given in Equation L15, where L represents the 1000 ft length of the lap as stipulated in competition rules.

$$t_l = \frac{2L}{V_c} \tag{34}$$

Equation L16 calculates the time taken in banked flight to complete the two 180 degree turns and a 360 degree turn in the lap. A 60-degree banked turn is used to calculate the banked time, corresponding to a load factor n of 2.

$$t_b = \frac{4\pi V_c}{\sqrt{g(n^2 - 1)}} \tag{35}$$

The total time to complete missions 1 and 2 are then calculated as $3(t_l + t_b)$. Because the missions are evaluated at maximum speed which balances thrust and drag, the smaller mass does not affect the calculation significantly. The Mission 3 time includes a rough approximation of landing and takeoff performed at takeoff speed V_{TO}, and budgets a minute of time on the ground for payload delivery. The completion times are listed below, along with the intended payload, in Table 4.4.3.1.

Table 4.4.3.1 List of Preliminary Design Mission Performance Predictions

Variable	Meaning	Value
t_{M1}	Mission 1 Completion Time	2.12 min
t_{M2}	Mission 2 Completion Time	2.12 min
t_{M3}	Mission 3 Completion Time	4.17 min
-	Number of Syringes (M2)	36
-	Number of Payloads (M3)	3

§5 – Detailed Design

§5.1 – Subsystem Design

§5.1.1 – Propulsion

§5.1.1.1 - Components Selected

A combination of two XILO 2250 mAh lithium-polymer batteries connected to each motor was selected to provide the necessary capacity for Mission 2, explained in Section 4.2.2 Using eCalc to model our propulsion system, a maximum current of 14.3A was estimated to be drawn from each battery, so two Castle 25A ESCs were selected for a factor of safety of 1.7. Two Cobra 4012/30 motors and two 13x9 APC propellers were also chosen for our final design. Table 5.1.1.1.1 summarizes the propulsion system of the aircraft.

Table 5.1.1.1.1 Final electronic and propulsion configuration.

Components	Details
Battery	Two XILO 2250 mAh 6s 75C LiPo

ESC	Two Castle Creations Talon 25 Amp ESC
Motor	Two Cobra 4012/30 Multirotor Motors
Propeller	Two APC 13x9 Propellers

§5.1.1.2 - Integration and Layout

Regarding the integration and layout of the propulsion system, along with all the control surface and deployment mechanism servos, there were three items that needed to be integrated with the rest of the aircraft: the batteries, the ESC, and the motors. Figure 5.1.1.2.1 illustrates how each component is wired.

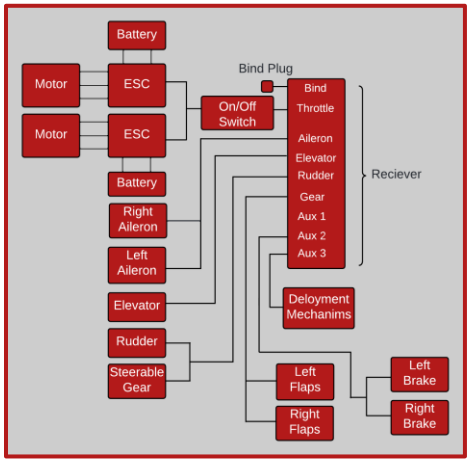

Fig. 5.1.1.2.1 Diagram of electronics system

The batteries for the aircraft are housed forward of the fuselage towards the nose of the plane. A large compartment was made so that the exact location of the battery could be moved around to adjust the overall center of gravity of the aircraft if necessary. This is done using Velcro strips running along the compartment. An arming/disarming switch is also located near the battery to further ensure that the battery does not supply power to the receiver when not intended.

The motors are attached to the wing using short carbon-fiber spars extruding from the wing. The use of carbon-fiber provides structural integrity for the wing, ensuring that the motor remains attached when providing large amounts of thrust to the aircraft. A 3D-printed motor mount (Figure 5.1.1.2.2) made with Onyx, a nylon-based material with chopped carbon fiber, was manufactured for the integration of the motor to the motor spar. Two holes of size 8-32 were drilled into the mount to screw into the motor spar for proper integration and stability.

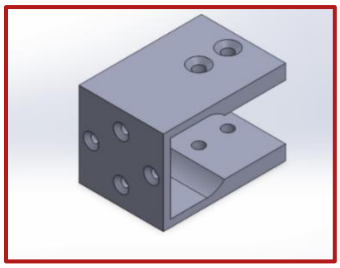

Figure 5.1.1.2.2 CAD render of motor mount

§5.1.2 – Fuselage

The fuselage is designed to store the optimum number of cargoes, based on sizing and scoring analysis. It is also designed to withhold electrical components while its geometry reduces the amount of aerodynamic drag it experiences during flight and takeoff. As depicted in figure 5.1.2.1 below, the fuselage contains a center carbon fiber spar while the fuselage's nose and aft are designed around this, tapering upwards. The carbon fiber spar is 0.9-inch in outer diameter and has a square cross section, adding to the structural integrity by resisting loading and torsion. The fuselage spar is positioned near the top to integrate the wing spar to the fuselage while maintaining the rigidity of both spars. The composition of the fuselage is mostly made of balsa wood, while interchanging some ribs with hardwood to increase the overall structural integrity of the fuselage. Stringers of 1/8-inch thickness and 1/2-inch width are extended along the length of the fuselage, attaching to the edges of connecting ribs. Their purpose is to provide a surface for MonoKote to wrap around and heat shrink against while providing some structural integrity. A side hatch is used to allow easy access for insertion or removal of any payload. A top-battery hatch is also used and is situated near the front of the fuselage to facilitate battery and electronics access. Both hatches are plates of wood that are secured to the fuselage by Velcro and hinge tape, cutting holes in the MonoKote to allow removal. Additionally, square holes are cut in the floorboard of the fuselage to constrain the vaccine vial packages within the fuselage while they drop off in the designated areas as the racks under them retract. To increase torsional rigidity of the fuselage, cross-shaped plates were designed and sandwich the fuselage spar - wing spar intersection, while being inserted into the ribs adjacent to the intersection. To integrate the tail, 1/16-inch-thick carbon fiber L-brackets were used to attach the empennage to the fuselage spar by use of screws. At the front of the fuselage a 3d-printed nose cone made of ABS plastic is attached by screws to the front face of the fuselage, whose purpose is to direct laminar airflow smoothly over the rest of the fuselage [9].

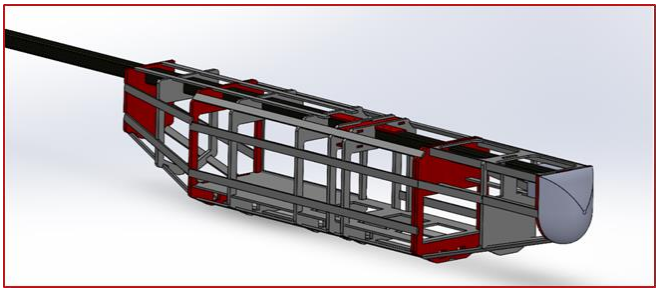

Figure 5.1.2.1 Image of Fuselage CAD

§5.1.2.1 – Fuselage Parameter Selection

Fuselage length, width, and height were mostly constricted by the number of syringes to be delivered in the second mission. Because ideation for the syringe holding mechanism began first, the number of syringes to be held per container determined how long to design the fuselage, resulting in a total length of 0.979 m with an internal cargo length of 0.495 m. Internal cargo width and height were also based on the syringe mechanism, having an internal width of 0.127 m and an internal height of 0.110 m. The external dimensions were determined based on structural integrity factors, where ribs and stringers can slot into and extend along the fuselage without hindering cargo. The total height of the fuselage is 0.186 m while the total width is 0.153 m. The nose region length of the fuselage was designed with the length of the propulsion batteries in mind, containing a nose length of 0.264 m. The tail was

designed to reduce separation of air flow from the body of the fuselage while retaining some geometrical symmetry of the fuselage, having a tail length of 0.181 m.

Fuselage rib placement and design were performed with a heavy emphasis on mass conservation. The centers of each rib are hollow while only the edges of each rib are sufficient to support the semi monocoque structure of the fuselage. To optimize mass savings, four hardwood ribs are used while six balsa ribs are used. Two of the hardwood ribs were positioned at the front-most and rear-most ribs to support the loads due to the empennage and the batteries, while the other two were interchanged between balsa ribs in the body of the fuselage. The nose ribs have battery hole cut outs while stringers support the weight of the batteries under them, slotting into the adjacent ribs.

§5.1.3 – Landing Gear

The landing gear was designed using the tricycle gear configuration. The tailwheel configuration was also considered, but due to the placements of the syringe racks and package dropping mechanism for mission 3 it was ultimately rejected. The tricycle design puts the plane level with the ground, which is needed for the successful performance of other aspects of the plane, while the tailwheel design puts it at an angle. This design required the placements of the wheels to be as close to an equilateral triangle as possible, with the back wheels being placed shortly behind the center of mass and under the wings. Unfortunately, due to the parts available to the team, the dimensions of the plane, and a desired height clearance of 2 inches between the propeller and the ground, a perfect equilateral triangle was unable to be formed. However, testing has shown that the plane is still extremely stable regardless. The design is shown in Figure 5.1.3.1.

The front gear, which was made from a wheel and servo, allows the plane to steer itself. A nose plate was manufactured and attached to the bottom of the nose for the gear to attach to. Originally, a different front gear was ordered that would have had the added benefit of being retractable. However, the order took a long time to arrive and was missing the wheels when it did arrive. Instead, parts that were already available to the team were used. The height and size of the scavenged wheel matched up well with the original design, only requiring a different integration method, which was fixed using the nose plate.

The back gear was made from a carbon fiber arch and two large polyurethane rubber wheels. A brake system was attached to allow for greater control over the plane. The wheels were chosen as their large size and material increased the ground stability of the aircraft and the gear's resistance to landing impacts. Similarly, the carbon fiber arch was chosen to absorb shocks better and take some of the landing loads off of the fuselage. The arch was also required to provide sufficient clearance for the packages to slip underneath the plane and between the wheels. Figure 5.1.3.1 displays a CAD of the full landing gear attached to the aircraft.

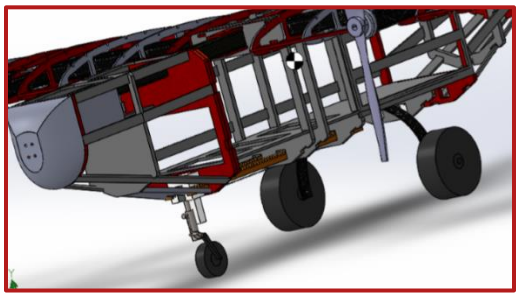

Fig. 5.1.3.1 CAD of the Landing Gear on the Aircraft

The brakes are modified from the E/Z Brakes System by DU-BRO, where a spring wraps around a cylinder that is attached to the wheel. The wire is attached to two separate servos, one for each side. As the servo is triggered, the spring tightens around the cylinder, slowing down the wheel. These brakes were chosen because they are light, affordable, and offers partial braking, which is advantageous when taxiing and turning the plane. The brakes were modified by installing screws to ensure the brakes would stay on the wheels after modifying them.

During testing, the landing gear proved to be very durable and stable. The primary goal for the gear was to build a strong, lightweight gear that was capable of steering and braking. The largest obstacles were the installation of the brakes, stabilization of the front gear, and integration of the front and back gears, with the solutions to each of these issues requiring a lot of engineering and creativity. Despite encountering a few obstacles, the landing gear was built well and accomplished all of the planned goals. Throughout many tests, the landing gear did not fail once and integrated with the rest of the aircraft exceptionally.

§5.1.4 – Wing

§5.1.4.1 - Overall Description

The wing is designed primarily to provide sufficient lift force for the aircraft with as many onboard syringes or vaccine packages as possible while ensuring the aerodynamic stability of the aircraft during various stages of all three missions. At the same time, the detailed structure of the wing is optimized to have minimized weight but still be able to sustain aerodynamic, bending, and torsional loads (Andrew J. Keane, 2017).

§5.1.4.2 - Detailed Dimensions

Table. 5.1.4.5.1 Table of Final Design Parameters

Parameter	Value
Aerodynamic Configuration	Conventional high wing
Airfoil	Clark Y
Wingspan	2.438m (8 ft)
Root Chord	0.3722 m
Tip Chord	0.2792 m
Mean Aerodynamic Chord	0.3280 m
Wing Surface Area	0.85 m2
Aspect Ratio	7.0
Taper Ratio	0.75
Wing Oswald Efficiency	0.84
Effective Aspect Ratio	5.87
Flap Surface Area	0.0414 m2
Flap Mean Chord	0.0846 m

Aileron Surface Area	0.0354 m2
Aileron Mean Chord	0.0748 m

Dimensions and general shape of the wing were mostly determined by the scoring analysis process. These dimensions are mostly unchanged throughout the design and initial manufacture of the first wing, except for slight adjustments to control surface area with the purpose of fitting the control surface between ribs in the main wing structure. In terms of aerodynamic design, the Clark Y airfoil was finally chosen for the first design because of its relatively high c_l/α ratio and high stall angle of attack. It is also easier to MonoKote and more reliable because of its convex shape. In terms of structural design, the general shape of the wing would be constructed with an interlocking assembly of wood ribs and wide stringers, as seen in Figure 5.1.4.2.4.

As for the specific materials, ribs that were expected to sustain loads and the wider stringers at the leading edge, as well as 3/4 chord, would be made with 1/8-inch-thick hardwood, while all other ribs and stringers will be made with 1/8-inch-thick balsa wood. Holes were added to all the ribs for weight-saving purposes while a tolerance limit of 1/4 inch was followed to ensure structural integrity. Those wood pieces will be glued together; if hardwood is involved, wood glue would be used, while if only balsa parts are involved, CA glue was used for the connection. A long square carbon fiber spar with a side length of 0.9 inches runs through each side of the wing along the wingspan, meeting at the middle of the aircraft, and it is fastened by screws to the fuselage. On each side, there is also one shorter spar with the same cross-sectional dimensions that is perpendicular to the main spar. It is connected to the main spar with two aluminum plates (one on the upper side and the other on the lower side), screws, and fasteners. Those two short spars serve as the connection between the wing spars and the motor mounts.

The control surfaces, including flaps and ailerons, have a similar design as the wing, except it has only one wide hardwood stringer and one balsa stringer to keep the shape of the assembly, as seen in Figure 5.1.4.2.2 below.

All the ribs on the control surfaces would be made with balsa. The connection between control surfaces and the wing would be done by gluing plastic hinges to the 3/4 chord stringer on the wing and the hardwood stringer on the control surface. Wood glue would be used for this connection. The hinges are not shown in the CAD model but they are clearly visible in Figure 5.1.4.2.3 below.

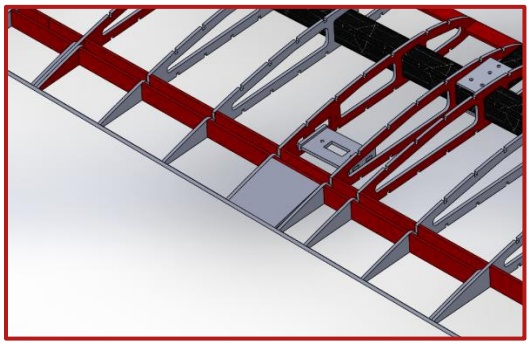

Fig. 5.1.4.2.2 Image of Control Surface Structure

Fig. 5.1.4.2.3 Image of Control Surface Hinges (circled)

In the initial design, servos for controlling the control surfaces are mounted on ribs with an acrylic servo mount and screws, and ribs on which the servos are mounted would be made with hardwood to ensure structural integrity. However, we later converted to using horizontal servo mounting plates (as shown in Fig. 5.1.4.2.2 above) because it does not require a long control horn and is also more secure. Each servo will use a control rod attached to a

control horn mounted on the respective control surface to exert control on the surface. Balsa plates are added between ribs on the control surfaces to allow for more secure control horn attachment, as shown in Fig. 5.1.4.2.2 above.

Additionally, the skin of the wing would be made with MonoKote film, which would cover almost the entirety of the wing. Extra thin straight balsa stringers, which are not shown in the CAD but will fit into the square slots on the ribs, would help hold the MonoKote skin in tension.

At this point, the design of the wing has been completed. A full CAD model is shown in Fig 5.1.4.4.2

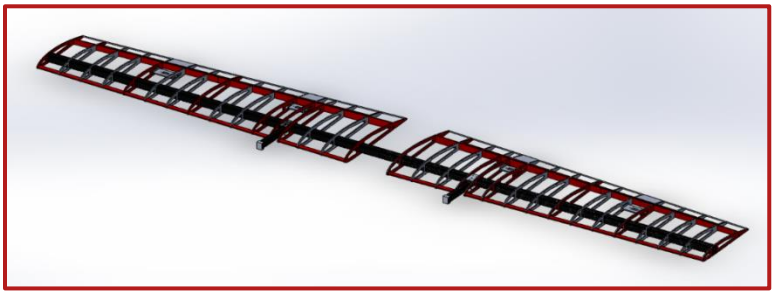

Fig. 5.1.4.2.4 Image of Full Wing Assembly

§5.1.4.3 – Wing-Spar Integration Bracket

It was challenging finding a ready-made T-bracket with the necessary dimensions for the integration between the wing spar and the motor spars. As a result, the team designed and machined brackets in our lab at Cornell University for the intended purpose. We opted for aluminum, more specifically 6061 Aluminum Temper-6 (often referred to as AL6061-T6), due to its strength, corrosion-resistance, and ease of manufacturing. Pictured below are the engineering and CAD drawings of the machined Aluminum brackets in Fig. 5.1.4.3.1, followed by design justifications.

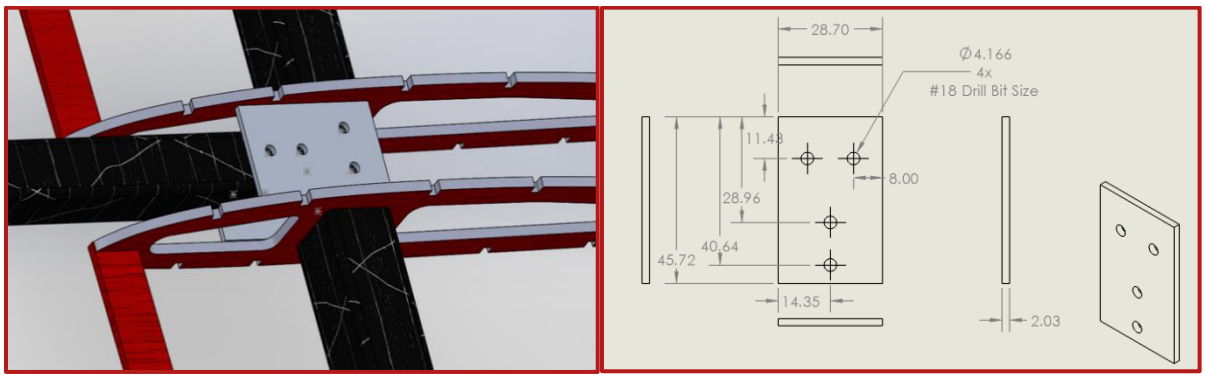

Fig 5.1.4.3.1 CAD and engineering drawings of Aluminum Bracket

The integration bracket is designed to fit between the wing's ribs, over the intersection between the wing spar and the motor spar. The 2 horizontally and 2 vertically aligned 8-32 screw holes lie on the wing carbon fiber spar and motor spar surfaces respectively. The decision to implement 4 screw holes in each bracket was prompted by the need for stability in the structure. With regards to the thickness of the bracket, a value of 2.03 mm (about 0.08 in) seemed ideal, with the reason being that each intersection point was strongly secured with 2 aluminum brackets (above and below) while maintaining the structural integrity of our wing.

§5.1.5 – Tail

§5.1.5.1 - Overall Description

The tail is designed to provide sufficient lift while stabilizing the aircraft during flight. The tail helps the plane takeoff and maneuver in the air. It also serves to position the center of gravity near the center of lift. The tail is designed to minimize weight while being structurally stable and maximizing lift then maneuverability.

§5.1.5.1 - Initial design and Development

The initial dimensions of the tail were determined after the wing's dimensions so the tail could properly support the wing. The parameters for determining a tail configuration were weight, stability, drag, manufacturability, and integration. The tail sizing procedure started after the major parameters of the wing and fuselage were determined. The parameters of the tail were repeatedly tuned to achieve a static margin between 5%-15% for all three missions. The static margin was the measure evaluated to determine if the tail would make the plane more stable and less maneuverable or less stable and more maneuverable. All of the design parameters of the tail are shown in Table 5.1.5.1.1 and did not change for the final design.

Table 5.1.5.1.1 Tail Design Parameters

Parameter	Value
Aerodynamic Configuration	Conventional Tail
Airfoil	NACA0010
Horizontal Stabilizer Wingspan	0.716 m
Horizontal Stabilizer Chord	0.236 m
Horizontal Stabilizer Surface Area	0.170862 m^2
Horizontal Stabilizer Aspect Ratio	3
Elevator Chord	0.0590 m
Vertical Stabilizer Wingspan	0.3192 m
Vertical Stabilizer Root Chord	0.2600 m
Vertical Stabilizer Tip Chord	0.0810 m
Vertical Stabilizer Mean Aerodynamic Chord	0.2130 m
Vertical Stabilizer Surface Area	0.07652 m^2
Vertical Stabilizer Aspect Ratio	2
Vertical Stabilizer Taper Ratio	0.75
Rudder Chord	0.650 m

The configuration of the tail remained the same through iterations and the dimensions of the tail underwent only small adjustments. The NACA0010 airfoil was selected because of its symmetry, manufacturability, and heritability without much loss of lift. The structural design of the tail followed a similar process to the wing being constructed with an interlocking assembly of wood ribs and stringers as shown in Figure 5.1.5.1.3

The tail was designed in SolidWorks to correctly size all parts. Most of the parts are not complicated and can be laser cut from the SolidWorks drawings. The ribs and stringers that would sustain loads were made with ⅛ inch-thick hardwood for structural stability. The parts that would sustain the most load are the tip, base, and servo ribs of the stabilizers as well as the leading, ¾ chord, and trailing stringers. The base plate of the tail is made of hardwood as it holds the weight of the horizontal and vertical stabilizers. The rest of the stringers and ribs were made of 1/8inch-thick balsa wood because it is less dense and saves mass. The ribs of the horizontal stabilizer have holes to reduce mass so that the servo wires can trail through the horizontal stabilizer to the base plate. The servo ribs are located near the center of the ribs. There are holes in the vertical stabilizer's ribs so a dowel can be used as a stringer for the horizontal stabilizer. The dowel rod and rudder assembly are shown in Figure 5.1.5.1.4.

Fig. 5.1.5.1.3 Horizontal Stabilizer During Assembly

Fig. 5.1.5.1.4 Rudder During Assembly

All the wood was glued together with wood glue for its strength. When only balsa wood is used CA glue is used for the speed it dries. The horizontal stabilizer was constructed by first lining up the ribs. They are held in line with the leading and trailing stringers which are the first ones glued. The two sides of the horizontal stabilizer are then glued to the base plate. The vertical stabilizer is assembled with the same process. A dowel is put through the vertical stabilizer to help keep it together. Plates are glued on the control surfaces in locations corresponding to the servo locations on the stabilizers. The control surfaces are then attached to the respective stabilizers with hinges and glue. Then the servos are connected to the control surfaces with a control rod. After the tail is finished, it is attached to the tail spar with two L brackets that are screwed to the spar and the base plate. The screws are bolted because the stress on them is relatively low [11]. Figure 5.1.5.1.5 shows how the tail is integrated to the tail spar.

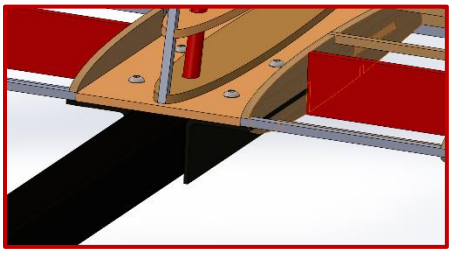

Fig. 5.1.5.1.5 Integration of Tail to Tail Spar

§5.1.5.1 - Iterated Design and Development

While the tail was being assembled improvement design improvements were made. Attaching the servos directly to ribs required large servo heads, so brackets were designed so that the servos could be attached parallel to the control surfaces. The brackets were made as I-brackets to maximize surface area with the ribs for gluing. The servo wires for the vertical stabilizer could not be threaded through because the ribs had no holes, so square holes were added so they could be. The holes were made to match the size of the servo wires, so little structural integrity was lost. Figure 5.1.5.1.6 shows how these changes were implemented in the rudder.

The tail base plate was bending under the weight of the horizontal stab. A T bracket was cut out of hardwood to be glued to the trailing edge of the horizontal stabilizer, vertical stabilizer, and base plate. This bracket prevents the bending of the baseplate, connects all of the tail, and increases the tail's overall rigidity. The singular wooden rod was not strong enough to connect the elevators by itself. A secondary smaller metal rod was used to connect the elevators as well to reinforce the connection between the elevators. The elevator rods and the Tail integration bracket are shown in Figure 5.1.5.1.7.

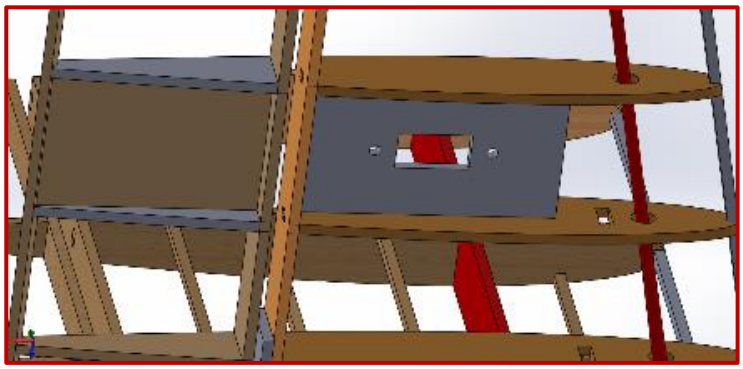

Fig. 5.1.5.1.6 Rudder Servo Integration Plate and Servo Wire Holes Fig. 5.1.5.1.7 Tail Integration T bracket and Second Elevator Rod

After analyzing the plane in AVL using values found experimentally the CG was found to be too far forward leading to a static margin of 28%. The tail spar was extended along with moving the tail back the same distance to help move the CG back to achieve a static margin of 5%-15%. The final tail design is shown in Figure 5.1.5.1.8.

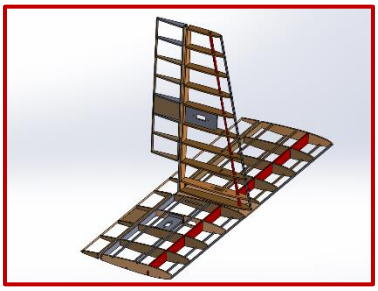

Fig. 5.1.5.1.8 Full Tail Assembly

§5.1.6 – Mission 2 Syringe Rack

The racks used in Mission 2 were designed to be lightweight, simple to manufacture, and easy to load with 30 mL syringes. To accomplish these goals, each rack is made of a 3D printed slab with specially sized holes to allow the syringes to be press-fit into it. The device is manufactured using ABS plastic. Of the plastics available, ABS was chosen because it is lighter and stronger than PLA. While the toughness of the material is not particularly critical given the very small loads supported by the device, it was optimized to save weight while sacrificing minimal structural integrity. The team also has access to resin printers, but the extra detail provided by this material would be unnecessary for this application, especially given their limited availability.

As shown in Figures 5.1.6.1 and 5.1.6.2 the main slab is supported by 3D printed legs that slot into the bottom of the rack and allow it to sit upright inside the aircraft. The legs are long enough to stretch across gaps made in the fuselage for Mission 3. Velcro strips allow the legs to attach to the fuselage baseplate to hold the rack in place.

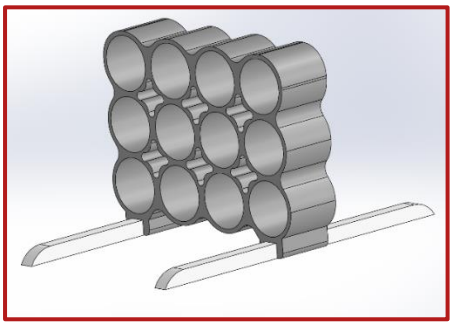

Fig. 5.1.6.1 CAD model of fully assembled rack

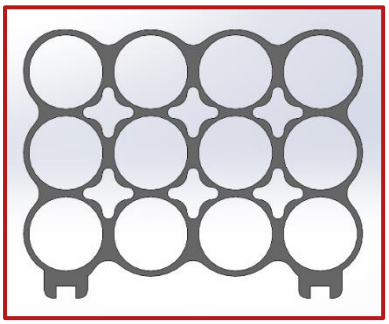

Fig. 5.1.6.2 Front view of rack slab

The number of syringes held by the device was dictated by preliminary scoring analysis, fuselage size, and weight concerns. Before designing the rack, the team used a MATLAB script to determine the optimal number of Mission 3 packages to maximize our score while considering weight and propulsion limitations. The team determined that the desired number was three packages, meaning a minimum of 30 syringes needed to be carried during Mission 2 (as dictated by competition rules). These factors led to each rack carrying 12 syringes with the entire aircraft carrying three racks for a total of 36 syringes, as specified in requirements SYS 1 and MECH 3. The syringe location within the fuselage is shown in Figure 5.1.6.3. This meets the minimum requirement needed for the team's Mission 3 configuration, as specified in requirement SYS 2, while also storing 6 extra syringes for an increased score without requiring large fuselage or propulsion system adaptations.

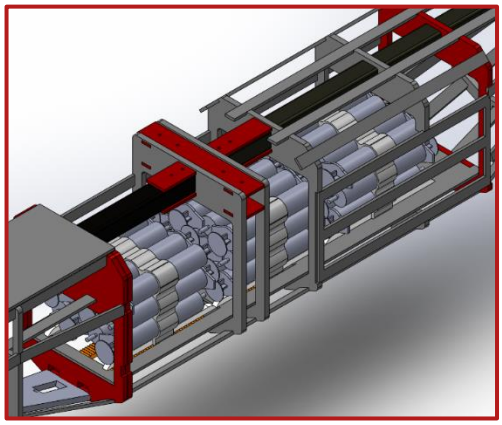

Fig. 5.1.6.3 Racks inside the fuselage

§5.1.7 – Mission 3 Package Deployment Mechanism

The package dropping mechanism, which is used in Mission 3, is designed to provide a reliable way of dropping vaccine vial packages while being simple enough to have consistent results that are easily analyzed. The design revolves around a rack and pinion system, where the vaccine vial packages rest on top of the racks. The components involved are a servo motor, a servo mount, two racks, a pinion, and a rubber band. Figures 5.1.7.1 and 5.1.7.2 shows the initial setup of the package dropping mechanism, with the fuselage baseplate and vaccine vial packages in their respective places at the start of Mission 3. The packages are colored tan, and the rack and pinion are orange.

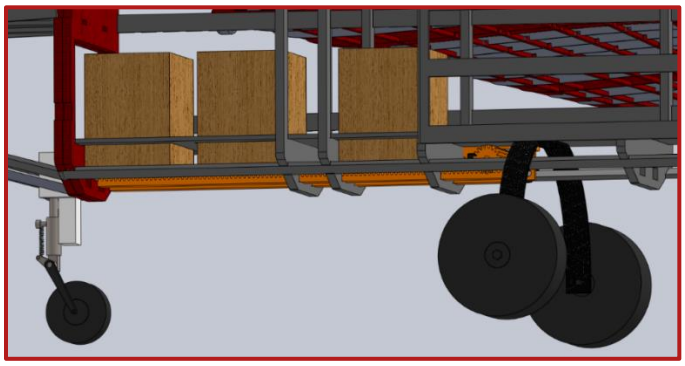

Fig. 5.1.7.1 Package Dropping Mechanism CAD

The vaccine vial packages initially rest in rectangular cavities in the fuselage baseplate, which constrain their lateral motion as the baseplate is near the package's midline. They rest on top of the two racks, which act as a floor that holds them within the fuselage. The racks, which rest in slots in the fuselage ribs, are located towards the bottom of the fuselage. The racks are driven by a pinion, which is powered by a servo. The racks are moved so that one by one, they will no longer support the packages from beneath. This exposes the packages to the ground with no support, resulting in them being dropped from the fuselage. Lastly, there is a rubber band running along the bottom of the fuselage's length. The rubber band is shown in gray between the two orange racks in Figure 5.1.7.2. It is located along the midline. Its purpose is to lessen the impact that the package experiences by converting some of the package's energy into elastic energy absorbed by the rubber band. Thus, the package will have less total energy upon impact, lessening the shock.

Fig. 5.1.7.2 View from the Bottom of the Fuselage CAD

§5.2 – Weight and Balance

SolidWorks is used to estimate the masses of each mechanical, structural, and electrical component of the aircraft. The program calculates the center of gravity of each component using various known densities and can compute the center of gravity of sub-assemblies and large assemblies. All CG values are taken according to a reference point set at the top-edge midpoint of the front face of the fuselage nose cone rib. The x-axis is defined along the fuselage of the aircraft, the y-axis is defined along the vertical height of the aircraft, and the z-axis is defined parallel to the wings. Table 5.2.1 displays the estimation for the location and magnitude of the center of gravity of each component of the aircraft.

In Table 5.2.1, there are a few components that have many subcomponents that are not explicitly listed. A common subcomponent are the associated ribs and stringer with the part. The Fuselage includes the fuselage carbon fiber

spar, and wing integration pieces. The Wing refers to both the left and right wing, and includes the wing carbon fiber spars, ailerons, flaps, motor spars, and servo brackets. The Vertical Tail includes the servo mount and rudder. The Horizontal Tail includes the servo mount, elevator, and tail integration piece. The Rear Gear includes the carbon fiber arch, two landing gears, and two wheels. The Nose Gear includes a metal rod, integration piece, and a wheel.

Table 5.2.1 Weight and Balance Table for All Flight Missions about the Front Fuselage Rib

Component	Mass (grams)	CG_x (meters)	CG_y (meters)	CG_z (meters)
Fuselage	951.9	0.43	0.05	0.01
Wing	765.67	0.47	-0.20	0.00
Vertical Tail	45.28	1.88	0.17	0.00
Horizontal Tail	95.88	1.85	0.00	-0.02
2x Batteries	634	0.05	-0.04	0.00
Receiver	9.4	0.33	-0.13	0.00
2x ESC	35.8	0.26	-0.14	0.00
2x Motors	280	0.26	-0.01	0.00
2x Propellers	139.2	0.25	-0.01	0.00
Nose Gear	105.57	0.24	-0.21	0.00
Rear Gear	423.49	0.60	-0.24	0.00
6x Control Surface Servos	38.25	1.00	0.04	-0.01
2x Rear Landing Gear Servos	15.3	0.63	-0.15	0.00
Front Landing Gear Servo	9	0.22	-0.16	0.00
Vaccine Package Dropping Mechanism	160.75	0.54	-0.17	-0.02
M1				
Total	3709.49	0.43	-0.08	0.00
M2				
3x Rack and Syringes	749.22	0.49	-0.10	0.00
Total	4458.71	0.44	-0.08	0.00
M3				
3x Vaccine Vial Packages	722.67	0.39	-0.13	0.00
Total	4432.16	0.42	-0.09	0.00

§5.3 – Flight Performance Parameters

The primary causes of difference in the flight performance parameters in the detailed design of Section 5 as compared to the preliminary design of Section 4 are the change in airfoil to the Clark Y airfoil, the inclusion of flaps and the more accurate mass and inertia modeling. The inertia matrix is taken from the Solidworks CAD model, and the final mass and position of center of gravity are obtained experimentally by weighing and balancing the aircraft. This allows the flight performance predictions shown below to be far more accurate than the predictions of Section 4. The inclusion of flaps was initially designed using techniques from the USAF Stability and Control DATCOM [12] document written by the McDonnell Douglas Corporation for the Air Force Flight Dynamics Laboratory. The team used a slightly modified version of the DATCOM empirical trends that was cited in Raymer's textbook [3], and for the simple plain flaps design that the team used for the detailed design, Equation L1 below calculates the increase in coefficient of lift expected for a given flap deflection.

$$\Delta C_L = 0.9K' \left(\frac{\partial C_L}{\partial \delta_f}\right) \frac{S_{flap}}{S} \delta_f \tag{36}$$

The parameters K' follows an empirical trend for flap effectiveness, $\frac{\partial C_L}{\partial \delta_f}$ describes the gain in lift coefficient as a function of flap deflection, the surface area ratio $\frac{S_{flap}}{S}$ describes the portion of the wing area used as the control surface, and δ_f describes the flap deflection. The increase in lift was calculated at 10-, 20- and 30-degree flap

deflections for an initial estimate of lift performance using hand calculations. These estimates showed a gain of 0.82 in lift coefficient for a flap deflection of 20 degrees, which is a very optimistic prediction but assists in the initial prediction of takeoff performance. The results shown below use AVL to model the lift and drag changes due to flap deflections at 20 degrees, and further flight testing shall be performed to determine the optimum flap deflection to allow for short takeoff and does not inhibit climb rate. Because the flap deflections affect the lift and drag of the main lifting surface, and the more accurate mass and inertia modeling removes a large amount of uncertainty present in the preliminary design, the stability derivatives for takeoff with flaps and cruise without flaps are shown for mission 1 with the empty payload and mission 2 with the full payload. Table 5.3.1 describes the expected aircraft performances in the empty payload mission M1 and loaded missions M2 and M3 in both takeoff and cruise configurations. Tables 5.3.2 list the stability derivatives of the aircraft in the same mission categories in takeoff and cruise condition.

Table 5.3.1 List of Aircraft Performances and Specifications in Various Configurations

Variable	Meaning	Performance, empty (M1)	Performance, MTOW (M2, M3)
m	Total Aircraft Weight	3.77 kg	4.62 kg
$C_{L_{\max}}$	Maximum Lift Coefficient (No Flaps)	1.26	
$C_{L_{\max,f}}$	Maximum Lift Coefficient (Flaps)	1.66	
V_s	Stall Speed	8.03 ms^{-1}	8.89 ms^{-1}
$V_{s,f}$	Stall Speed (Flaps)	6.98 ms^{-1}	7.75 ms^{-1}
V_{TO}	Takeoff Speed (Flaps)	9.07 ms^{-1}	10.08 ms^{-1}
V_c	Cruise Speed (Maximum Speed)	29 ms^{-1}	29 ms^{-1}
C_{L_g}	Takeoff Lift Coefficient	0.71	0.98
-	Takeoff Lift Force	30.5 N	51.74 N
C_{D_g}	Takeoff Drag Coefficient	0.12	0.14
-	Takeoff Drag Force	5.0 N	7.50 N
C_{L_c}	Cruise Lift Coefficient	0.085	0.101
-	Cruise Lift Force	37.0 N	44.2 N
C_{D_c}	Cruise Drag Coefficient	0.09	0.09
-	Cruise Drag Force	39.5 N	39.5 N
L_r	Takeoff Runway Length	4.63 m	7.33 m
-	Maximum Crosswind Capability	4.59 ms^{-1}	5.40 ms^{-1}
F	Takeoff Thrust	39.4 N	
TWR	Thrust to Weight Ratio	1.07	0.87
Re	Operating Range of Reynold's Numbers	$1.8 \times 10^5 < \mathrm{Re} < 6.9 \times 10^5$	

Table 5.3.2 List of Stability Derivatives for Detailed Design

Stability Derivative	Meaning	M1 Takeoff Condition	M1 Cruise Condition	M2, M3 Takeoff Condition	M2, M3 Cruise Condition
C_{L_α}	Lift force due to angle of attack (lift curve slope)	4.92	4.99	4.82	4.99
C_{m_α}	Pitch moment due to angle of attack (function of static margin)	-0.451	-0.345	-0.512	-0.352
C_{y_β}	Lateral force due to sideslip (yaw damping)	-0.267	-0.260	-0.270	-0.260
C_{l_β}	Roll moment due to sideslip (dihedral effect, spiral stability)	-0.060	-0.025	-0.079	-0.026
C_{n_β}	Yaw Moment due to sideslip (route stability effect, yaw feedback)	0.154	0.150	0.161	0.151

C_{y_p}	Lateral force due to roll velocity	0.087	-0.018	0.157	-0.012
C_{l_p}	Roll moment due to roll velocity (roll mode damping)	-0.475	-0.479	-0.467	-0.478
C_{n_p}	Yaw moment due to roll velocity	-0.032	0.006	-0.060	0.004
C_{y_r}	Lateral force due to yaw velocity	0.326	0.324	0.322	0.325
C_{l_r}	Roll moment due to yaw velocity (yaw/roll coupling)	0.147	0.065	0.196	0.068
C_{n_r}	Yaw moment due to yaw velocity (yaw damping)	-0.195	-0.188	-0.203	-0.189
SM	Static Margin	9.2%	6.9%	10.0%	7.17%

The tabulated values show that the static margin target of 5% to 15% has been satisfied, and the correct signs and magnitudes close to unity of each stability derivative (except for lift curve slope) predict conventional, manageable flight characteristics. However, a key concern remains that the spiral stability criterion was calculated to be lower than ideal and suggests that the aircraft may tend to spiral out of controlled flight. Another limitation of the analysis lies in the drag modeling. The very basic drag modeling of the aircraft does not consider fuselage effects and therefore severely underestimates the aircraft's drag properties, which results in an excessively high cruise speed. The aircraft still satisfies the short takeoff requirements but has a low contingency runway length and factor of safety.

§5.4 – Mission Performance

The mission performances are calculated using the same techniques as mentioned in Section 4 and are omitted from this section for brevity. Because the final mass of the aircraft is very similar to the predicted mass range from the initial sizing analysis techniques, and the thrust has not changed, the mission performances are almost identical.

Table 5.4.1 List of Preliminary Design Mission Performance Predictions

Variable	Meaning	Value
t_{M1}	Mission 1 Completion Time	2.12 min
t_{M2}	Mission 2 Completion Time	2.12 min
t_{M3}	Mission 3 Completion Time	4.11 min
-	Number of Syringes (M2)	36
-	Number of Payloads (M3)	3

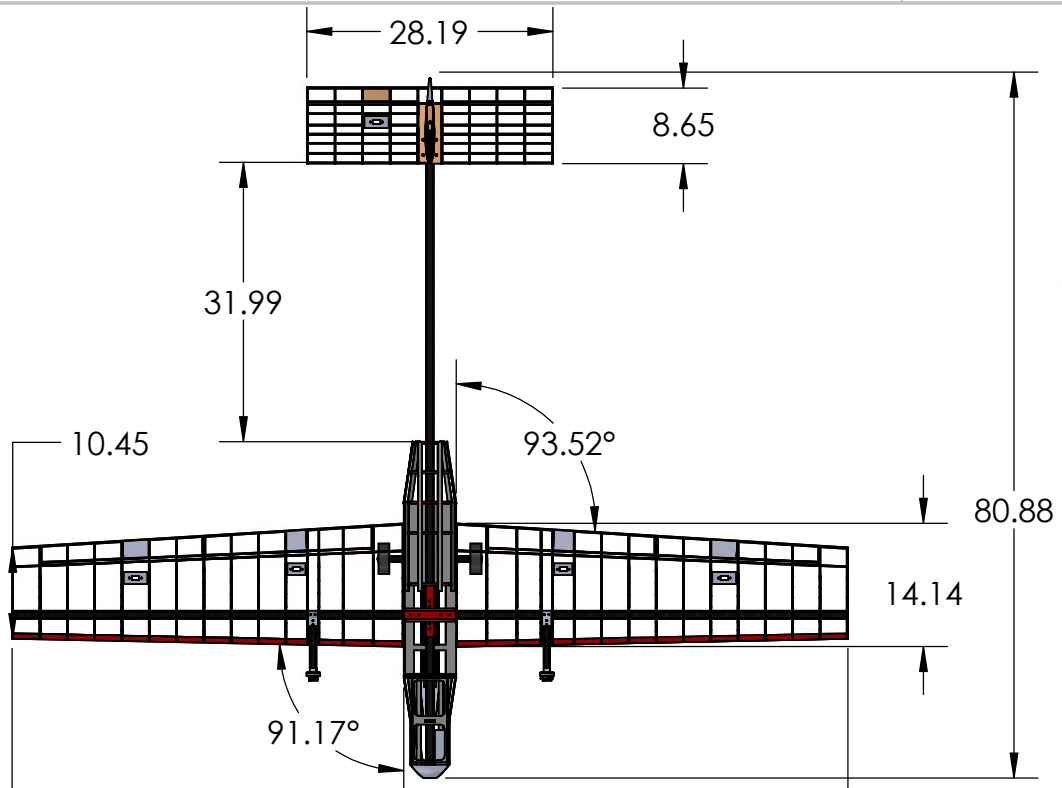

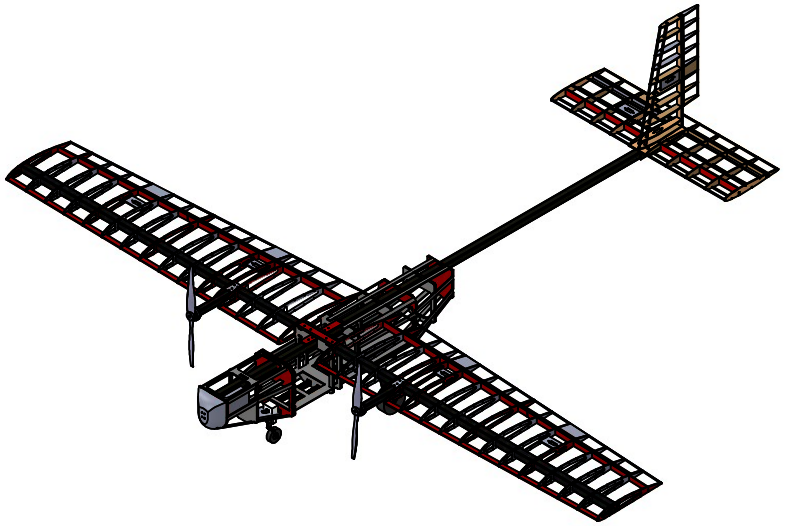

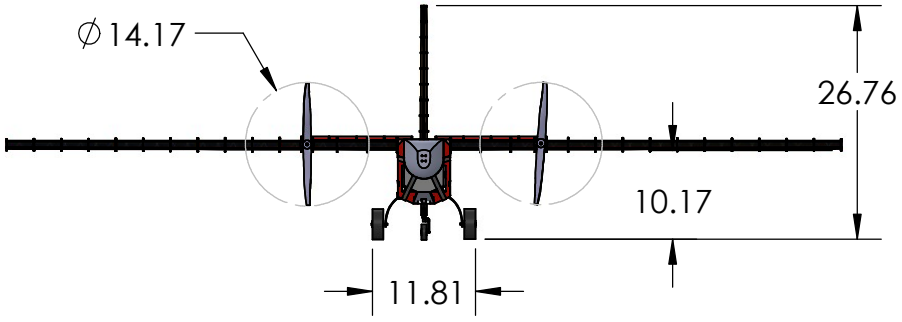

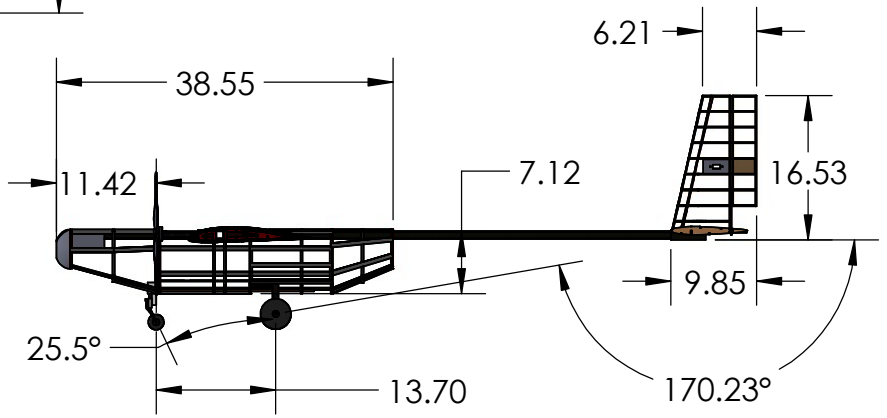

TOP SECRET			
THE INFORMATION CONTAINED IN THIS DRAWING IS THE SOLE PROPERTY OF CORNELL DESIGN-BUILD-FLY PROJECT TEAM. ANY REPRODUCTION IN PART OR AS A WHOLE WITHOUT THE WRITTEN PERMISSION OF CORNELL DBF IS PROHIBITED.		NAME	DATE
UNLESS OTHERWISE SPECIFIED: DIMENSIONS ARE: Inches <Meters> TOLERANCES IN INCHES: TWO PLACE DECIMAL ± THREE PLACE DECIMAL ±	Designer	Will Campisi	Will Kully
	Subteam Lead	Neil Ramasray	
Material Color Code: Hardwood, Red Balsa, Grey 3D Printed Plastics, Orange Acrylic, Translucent White Carbon Fiber, Black Electronics, Yellow			
DO NOT SCALE DRAWING			

TITLE:

Cornell University Design Build Fly Three View Drawing

SIZE	DWG. NO.	REV
A	1	
SCALE: 1:22		SHEET 1 OF 1

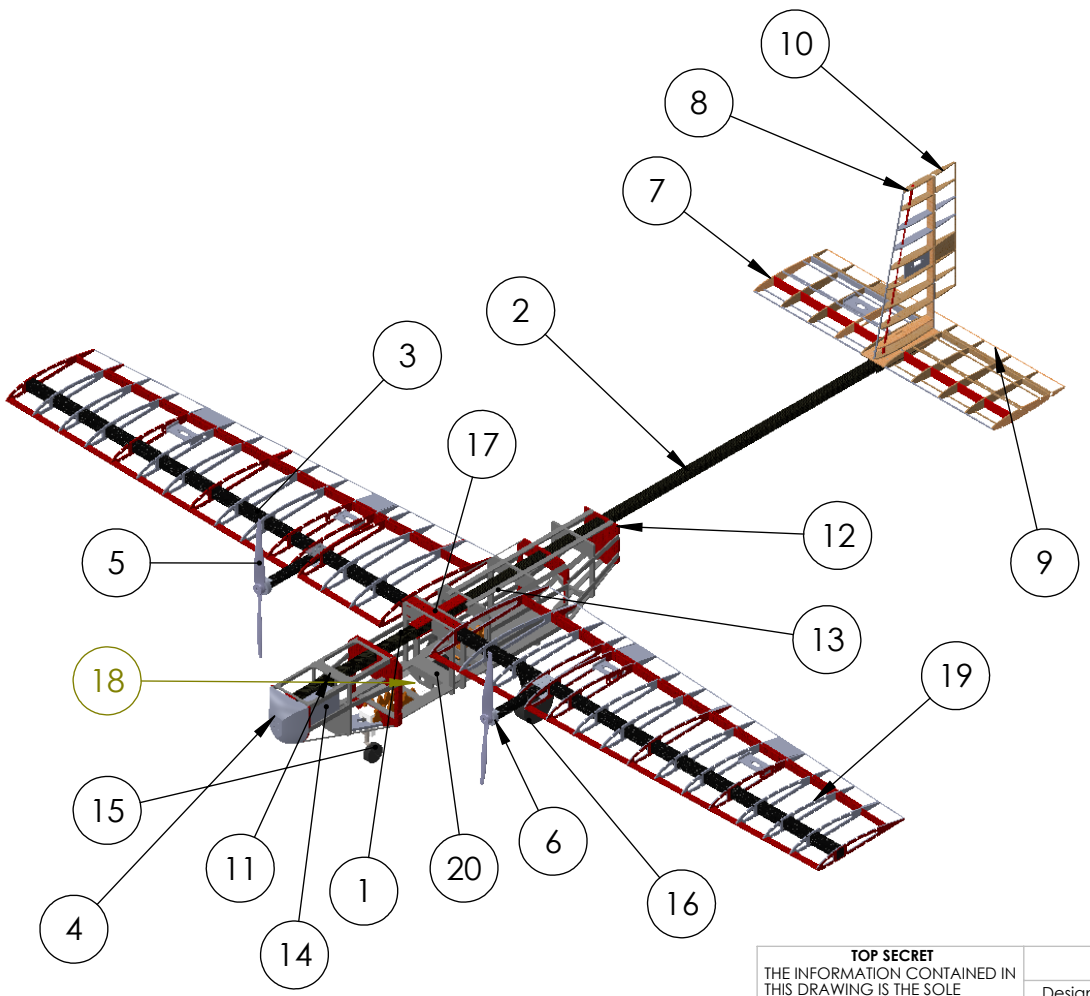

ITEM	DESCRTPITON	Qty.	MATERIAL
1	Fuselage Spar	1	Carbon Fiber
2	Tail Spar	1	Coarbon Fiber
3	Wing Spar	1	Carbond Fiber
4	Fuselage Nose	1	ABS Plastic
5	Propeller	2	Plastic
6	Motor	2	N/A
7	Horizontal Tail Frame	1	Balsa and Hard Wood
8	Vertical Tail Frame	1	Balsa and Hard Wood
9	Elevator	1	Balsa and Hard Wood
10	Rudder	1	Balsa and Hard Wood
11	Battery Cover	1	Balsa
12	Fuselage Ribs	10	Balsa and Hard Wood
13	Stringers	42	Balsa
14	Battery	1	N/A
15	Front Landing Gear	1	N/A
16	Rear Landing Gear	1	Carbon Fiber and Rubber
17	Wing Connector	2	Hard wood
18	Rack	2	ABS Plastic
19	Wing Ribs	32	Balsa and Hard Wood
20	Fuselage Floor Board	1	Hard Wood

UNLESS OTHERWISE SPECIFIED:
DIMENSIONS ARE: Inches <Meters>
TOLERANCES IN INCHES:
TWO PLACE DECIMAL ±
THREE PLACE DECIMAL ±

	NAME	DATE
Designer	Natalie Sun	Will Campisi
Subteam Lead	Christian Abbadessa	

Material Color Code:
Hardwood, Red
Balsa, Grey
3D Printed Plastics, Orange
Acrylic, Translucent White
Carbon Fiber, Black
Electronics, Yellow

DO NOT SCALE DRAWING

TITLE: Structural Arrangement

SIZE A | DWG. NO. 1 | REV

SCALE: 1:16 | SHEET 1 OF 1

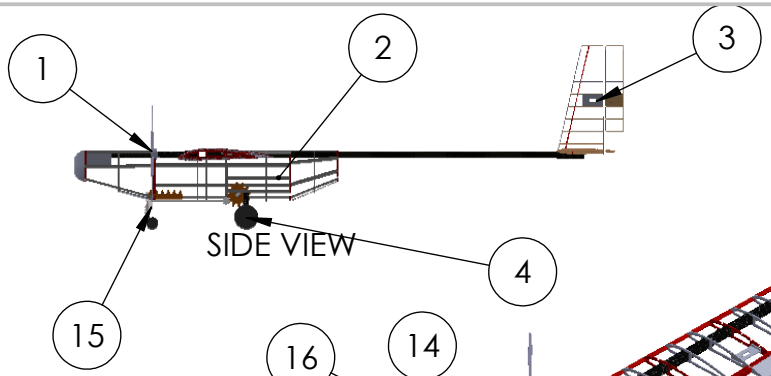

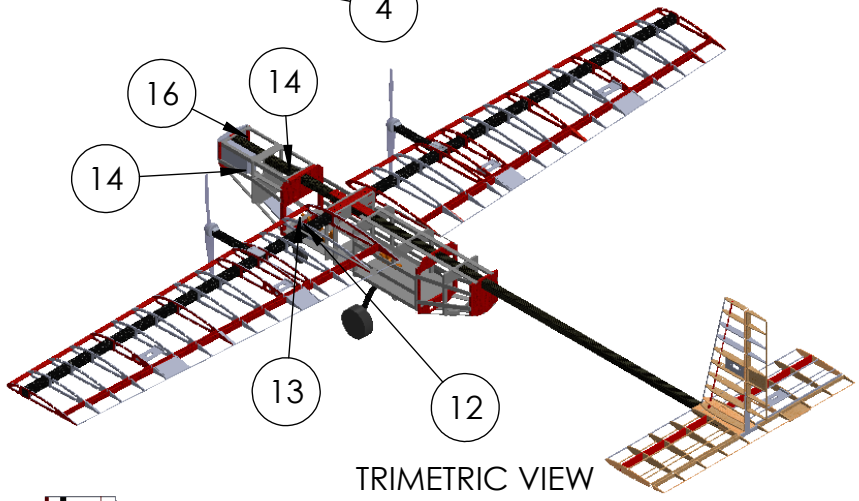

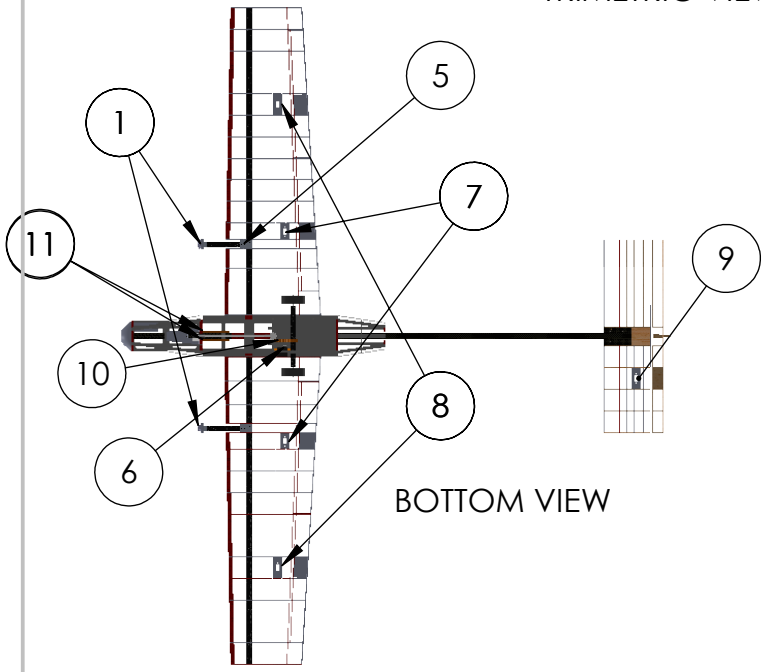

ITEM	DESCRIPTION	Qty.	SPECIFICATION
1	Propeller	2	13x9 APC Propeller
2	Side Hatch	1	Balsa and Velcro
3	Rudder Servo	1	Futaba S3114 Micro Servo
4	Rear Landing Gear Brake Servo	1	Futaba S3114 Micro Servo
5	Propeller Motor	2	Cobra CM 4012/30
6	Rack and Pinion Servo	1	Hitec HSR 2645CR
7	Flap Servo	2	Futaba S3114 Micro Servo
8	Aileron Servo	2	Futaba S3114 Micro Servo
9	Elevator Servo	1	Futaba S3114 Micro Servo
10	Pinion	1	ABS Plastic
11	Rack	2	ABS Plastic
12	ESC	2	Talon 25 ESC
13	Receiver	1	AR 8000 8-channel Receiver
14	Propulsion Batteries	2	XILO 2250 mAh 6S LiPo Battery
15	Front Landing Gear Steering Servo	1	Spektrum RC Aircraft Steering Servo
16	Battery Hatch	1	Balsa and Velco

UNLESS OTHERWISE SPECIFIED:
DIMENSIONS ARE: Inches <Meters>
TOLERANCES IN INCHES:
TWO PLACE DECIMAL ±
THREE PLACE DECIMAL ±

	NAME	DATE
Designer	Christian Abbadessa	
Subteam Lead	Neil Ramasray	

Material Color Code:
Hardwood, Red
Balsa, Grey
3D Printed Plastics, Orange
Acrylic, Translucent White
Carbon Fiber, Black
Electronics, Yellow

DO NOT SCALE DRAWING

TITLE:
SYSTEM LAYOUT

SIZE	DWG. NO.	REV
A	1	

SCALE: 1:16 | SHEET 1 OF 1

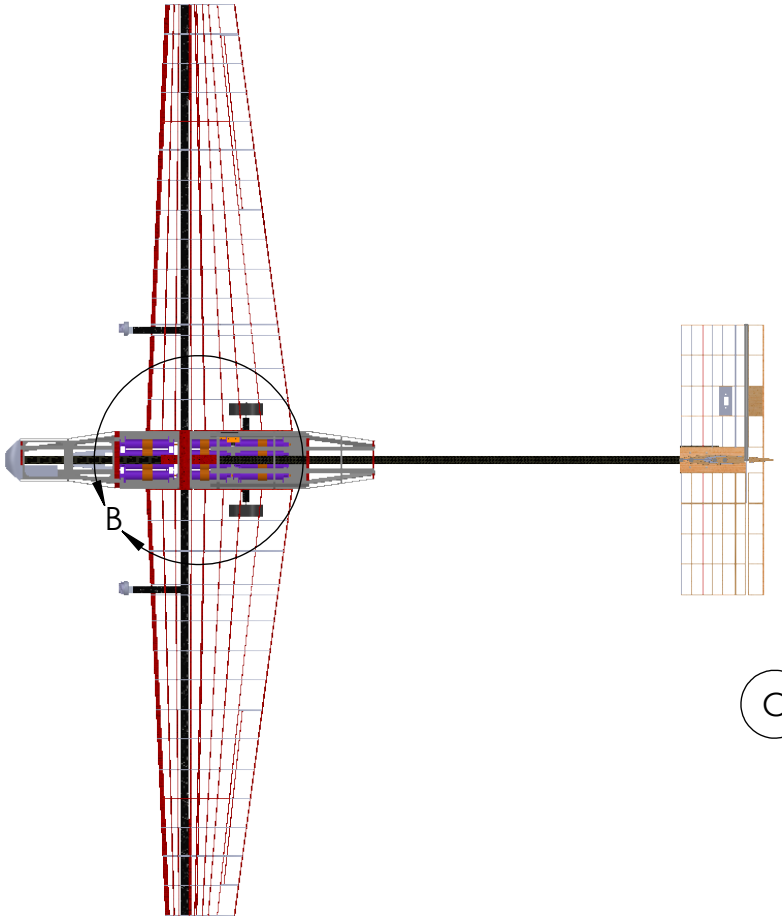

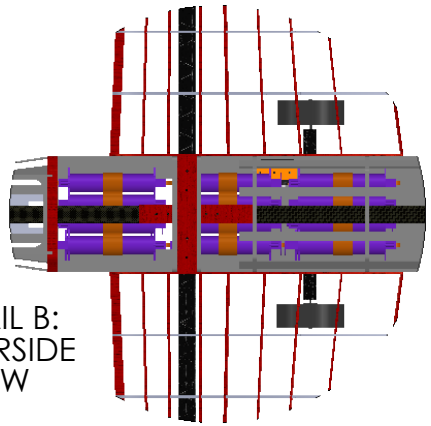

DETAIL B:
UNDERSIDE
VIEW

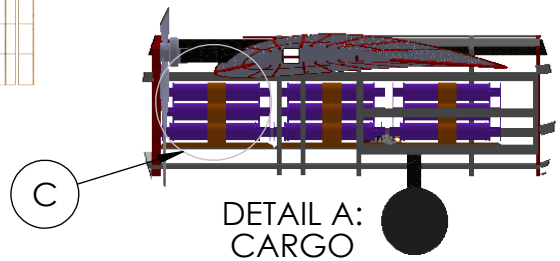

DETAIL A:
CARGO
VIEW

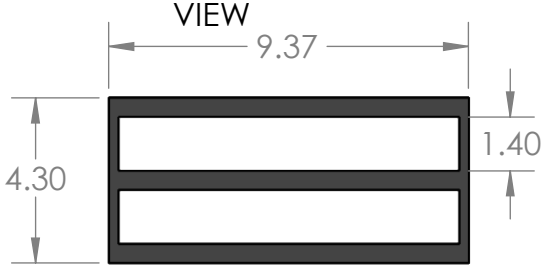

DETAIL D:
FUSELAGE SIDE HATCH

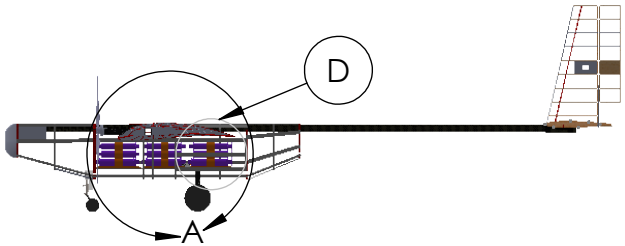

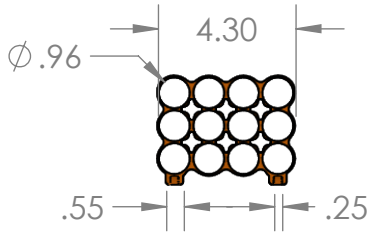

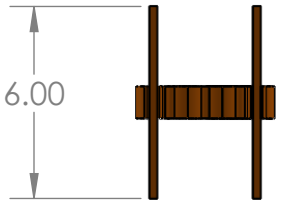

DETAIL C
SYRINGE RACK

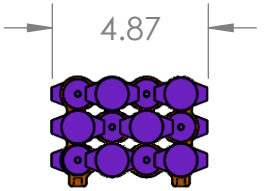

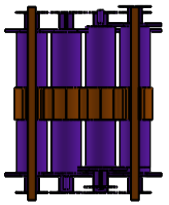

DETAIL C
SYRINGE RACK
WITH SYRINGES

TOP SECRET
THE INFORMATION CONTAINED IN THIS DRAWING IS THE SOLE PROPERTY OF CORNELL DESIGN-BUILD-FLY PROJECT TEAM. ANY REPRODUCTION IN PART OR AS A WHOLE WITHOUT THE WRITTEN PERMISSION OF CORNELL DBF IS PROHIBITED.

UNLESS OTHERWISE SPECIFIED:
DIMENSIONS ARE: Inches <Meters>
TOLERANCES IN INCHES:
TWO PLACE DECIMAL ±
THREE PLACE DECIMAL ±

	NAME	DATE
Designer	Christian Abbadessa	
Subteam Lead	Neil Ramasray	

Material Color Code:
Hardwood, Red
Balsa, Grey
3D Printed Plastics, Orange
Acrylic, Translucent White
Carbon Fiber, Black
Electronics, Yellow

DO NOT SCALE DRAWING

TITLE:
Mission 2 Payload

SIZE	DWG. NO.	REV
A	1	

SCALE: 1:22 | SHEET 1 OF 1

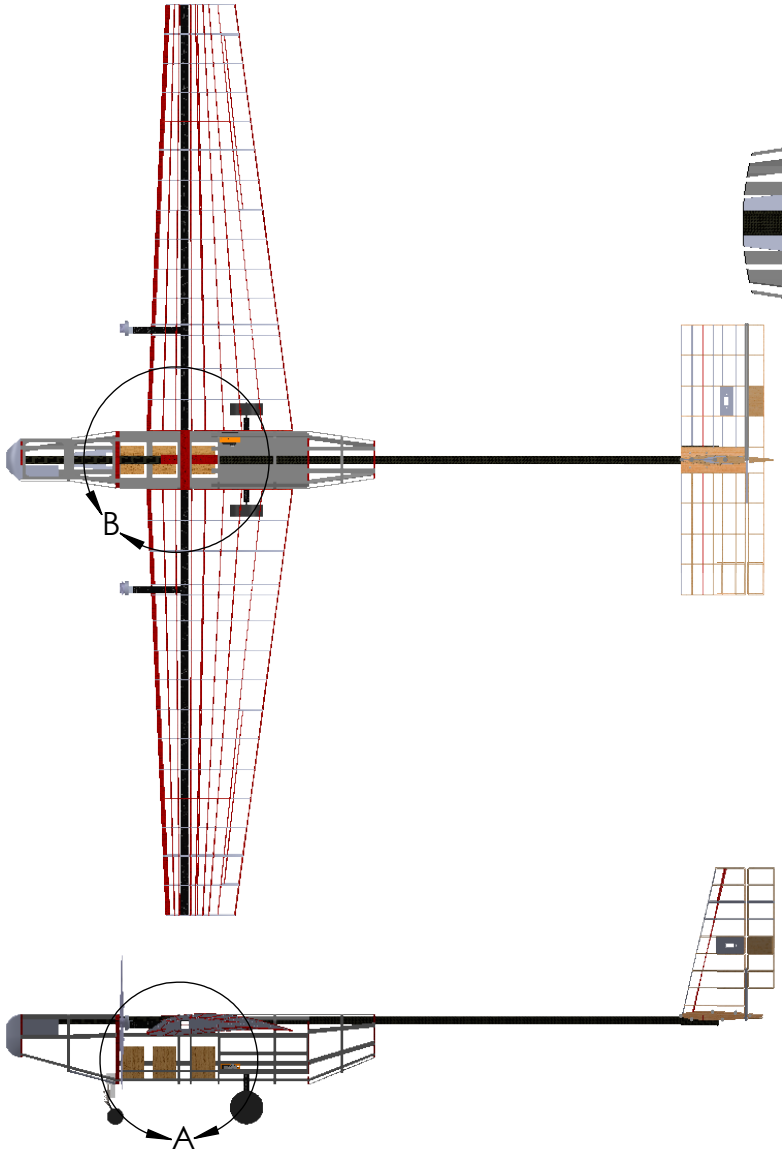

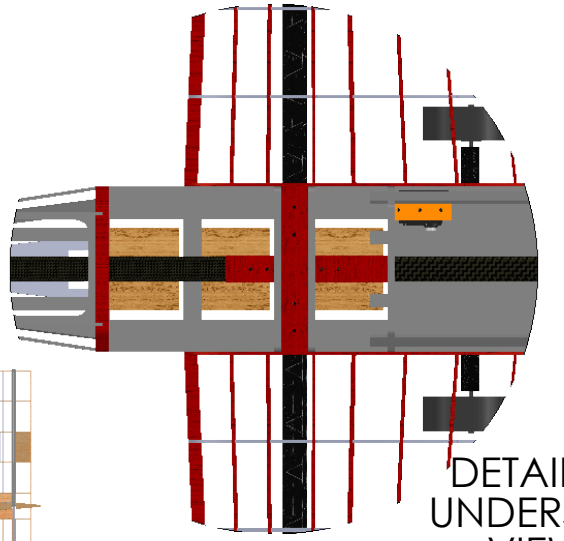

DETAIL B:
UNDERSIDE
VIEW

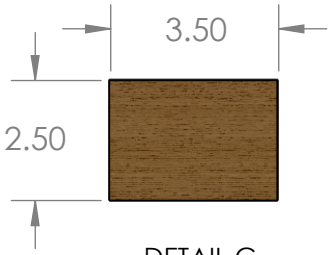

DETAIL C
SUBSTITUTE VACCINE VIAL PACKAGE

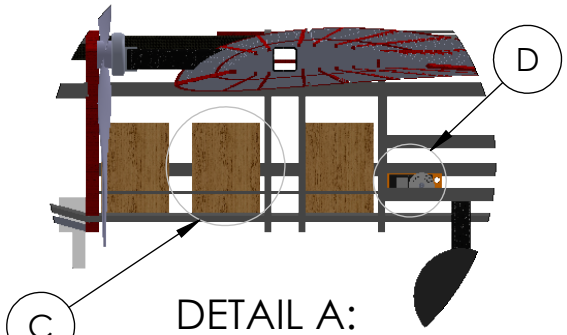

DETAIL A:
CARGO
VIEW

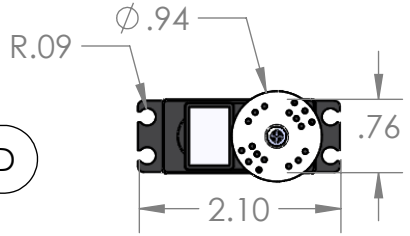

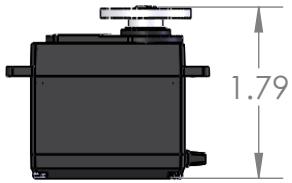

DETAIL D:
Hitec HSR 2645CR SERVO

TOP SECRET
THE INFORMATION CONTAINED IN THIS DRAWING IS THE SOLE PROPERTY OF CORNELL DESIGN-BUILD-FLY PROJECT TEAM. ANY REPRODUCTION IN PART OR AS A WHOLE WITHOUT THE WRITTEN PERMISSION OF CORNELL DBF IS PROHIBITED.

UNLESS OTHERWISE SPECIFIED:
DIMENSIONS ARE: Inches <Meters>
TOLERANCES IN INCHES:
TWO PLACE DECIMAL ±
THREE PLACE DECIMAL ±

	NAME	DATE
Designer	Christian Abbadessa	
Subteam Lead	Neil Ramasray	

Material Color Code:
Hardwood, Red
Balsa, Grey
3D Printed Plastics, Orange
Acrylic, Translucent White
Carbon Fiber, Black
Electronics, Yellow

DO NOT SCALE DRAWING

TITLE:
Mission 3 Payload

SIZE	DWG. NO.	REV
A	1	

SCALE: 1:16 | SHEET 1 OF 1

§6 – Manufacturing Plan

§6.1 – Manufacturing Workflow

The team's manufacturing process, at a high level, consists of the following stages – fabrication, subsystem/component assembly, and aircraft integration – as depicted in Figure 6.1.1. Upon completion of the conceptual design phase, a CAD model is created in SolidWorks and reviewed, in a series of increasingly intensive and detailed design reviews, for all aircraft components and mechanisms. In the fabrication stage, those CAD models are used to create .dxf drawings for laser-cuts, or .stl files for 3D printed components. The majority of the aircraft structure, including fuselage, wing, and tail are laser-cut balsa and hardwood sheets, with 3D prints used for more complex geometries.

Those pieces, along with purchased components, such as the carbon fiber structural spar and servos, are then assembled into aircraft subsystems using epoxy, cyanoacrylate glue, or other hardware fasteners such as nuts and bolts in the subsystem/component assembly stage. The assembled subsystems and components are covered with MonoKote, as necessary to create a smooth, continuous exterior surface, before being integrated with the other components, including electronics and propulsion, in the aircraft integration stage. Mission-specific mechanisms, such as the vaccine package deployment system, are manufactured in a similar design, CAD, fabrication, assembly, and integration cycle, though additional ground testing is conducted prior to integration with the aircraft.

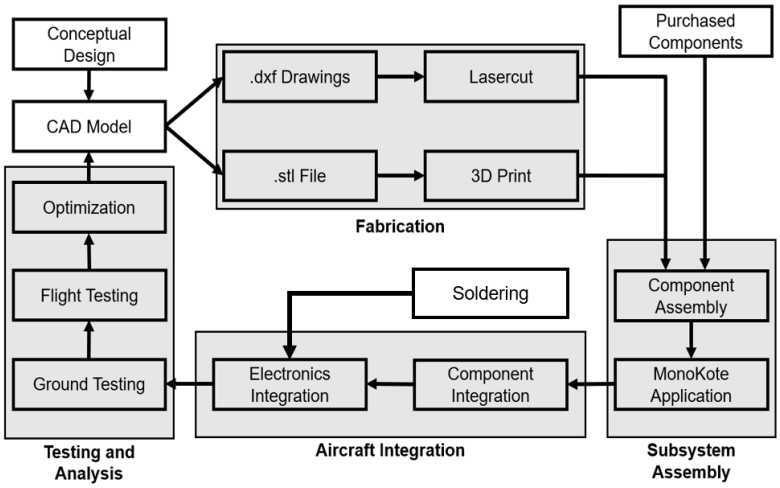

Fig. 6.1.1 – Manufacturing workflow diagram

§6.2 – Laser cutting

Using Cornell facilities, laser cutting was readily available to the team and became one of the primary means of construction for the many components of the aircraft. Two laser cutting machines were available of use, with the larger, more public machine having maximum wood board cutting dimensions of 36-inch by 6-inch. The smaller, more private laser cutter can cut maximum dimensions of 18-inch by 12-inch, so we were able to efficiently use our time and resources by alternating between laser cutting machines

Balsa and hardwood were the main materials chosen for laser cutting to provide a minimum amount of weight while maximizing structural integrity. For example, low-density balsa was used for stringers whose purpose is to connect

adjacent ribs within the fuselage, the wings, and the tail. It also provided a surface for MonoKote to wrap around to help minimize aerodynamic drag. On the other hand, hardwood was used more conservatively because of its higher mass density. It was inserted in areas where significant loading would be experienced to resist stress while minimizing total mass of each component. Most of the wood was 1/8-inch thick, which is the optimal thickness to handle loads while minimizing volume and mass for the specific purposes of this plane.

§6.3 – 3D printing

The primary additive manufacturing method used to create complex parts was 3D printing. Because of access to Cornell University's Rapid Prototyping Lab, the team had the ability to choose *between* ABS, PLA, resin, and even carbon fiber. ABS plastic was selected and used on all 3D printed parts for the plane because it was able to be strong enough to support needed loads at a low weight and infill percentage (~30%). ABS plastic is also perhaps the most common amongst 3D printing plastics, so it is relatively cheap and easy to obtain.

§6.4 – Landing Gear

The nose plate for the front gear was laser cut out of hardwood, with a hole for the servo mount being cut through the middle. The screw holes in the carbon fiber arch were drilled in Cornell University's ELL Composites Lab. Heat shrink was wrapped around the front gear to increase stability, as the front wheel would tilt at rest.

§6.5 – MonoKote Covering

MonoKote is a plastic shrink wrap that is used to cover surfaces on the exterior of the plane. Specifically, it was used to cover the exterior surfaces of the wing, fuselage, and tail. MonoKote was chosen because it allows the plane to be covered and streamlined for aerodynamic purposes, as lift force requires a surface to apply pressure onto. It is applied by first cutting sheets to size and then positioning them so that the edges are aligned with a firm surface on the plane. Then, an iron was used to attach the edges of the MonoKote to the plane. Lastly, a heat gun was used to heat shrink the MonoKote to create a streamlined surface.

§6.6 – Adhesives

There were 4 different adhesives used to manufacture the plane: Cyanoacrylate (CA), standard wood glue, epoxy, and Velcro. Cyanoacrylate was used for balsa-to-balsa wood connections. Wood glue was used to attach any other types of wood together. Epoxy was used to attach plastic components to the plane, specifically 3D printed parts like the nosecone. Velcro was used for pieces of the plane that had to be removed at various times, such as the battery hatch, main hatch, and the mission 2 racks.

§6.7 – Wing

The first phase of wing manufacture started immediately after most designs of the wing were done and all manufacturing-related files, including the laser cutting files of all wooden parts, were finished. As preparation for wing assembly, balsa and hardwood sheets were brought to the university's Rapid Prototyping Lab and were cut there into ribs and wide stringers. Then, those parts were assembled according to the CAD model and were temporarily held together by masking tape. The carbon fiber spar was run through the assembly to ensure that all the ribs were aligned correctly, and after alignment was checked and corrected, the tape was taken off and wood

glue was applied to connection points between wooden components. At this point, the general structure of the wing was completed. Thin balsa stringers were then cut with a stringer cutting tool and were then glued with CA glue to the wing, which readied the wing for monoKoting.

At the same time, the control surfaces were assembled: ribs and wide stringers were put together with matching slots and temporarily secured with masking tape, their alignment was checked by fitting the taped assembly into the slots on the wing, and after alignment is checked the assembly was glued with wood glue and CA glue. Wood servo mounting plates were also assembled and glued with wood glue to the ribs in this step, and the servos were first glued to acrylic servo mounts and then glued to servo mounting plates.

The following step was monoKoting, in which we used irons to attach monoKote films to the stringers and tightened the films with heat guns, therefore creating a smooth surface on the wing and the control surfaces. Then, carbon fiber spars were machined to adequate sizes according to the design, and holes are drilled on the spars for screws. The aluminum spar integration plate, which connects the main wing spars and the motor spars, was also cut to size and drilled at corresponding locations. The motor spars were then connected to the main spars with the integration brackets, screws, and washers. A few small parts of monoKote were broken open and then patched during this process in order to allow access to screw holes.

Attachment of control surfaces was done by gluing plastic hinges with wood glue to the wing 3/4 chord wide stringer on one side and the control surface wide stringer on the other. After that, plastic servo horns were screwed onto servos and control horns onto control surfaces. They were then connected with steel control rods, which were secured with screws on each horn. Each side of the wing was then connected to the fuselage by screwing the main wing spar with integration plates on the fuselage

§6.8 – Fuselage

To align the components in the correct position, all the wooden components were based off the central carbon fiber spar, constructing the fuselage from nose to tail. All other structural components were laser cut using Cornell's resources. Balsa and hardwood were assembled using adhesives, using cyanoacrylate to connect balsa components while wood glue was used for hardwood.

Balsa stringers were cut using a wooden strip cutter device that can cut wood at a certain length parallel to the wood. To hold the propulsion batteries with a greater safety factor, 0.25-inch-thick balsa stringers were used. Velcro was epoxied on the wooden ribs of which the hatches interfaced, and the hatches were secured even further with hinge tape. Screw holes were drilled into the baseplate for the back landing gear to integrate while servo holes were cut into the baseplate for the rear brake servos to slot into.

After structural assembly, a thin sheet of MonoKote was applied and heat shrunk around the fuselage using irons and a heat gun. To give the hatches full functionality, patches of MonoKote were cut out to allow insertion or removal of the hatch plates.

§6.9 – Tail

The tail was designed in SolidWorks to correctly size all parts. Most of the parts are not complicated and can be laser cut from the SolidWorks drawings. The horizontal stabilizer, vertical stabilizer, elevators, and rudder were

assembled separately as it makes it easier to cover them with MonoKote if done individually. The horizontal stabilizer was constructed by first lining up the ribs. They are held in line with the leading and trailing stringers which are the first ones glued. The servo integration plates are glued in between the ribs on the left side before the rest of the stringers are glued. The two sides of the horizontal stabilizer are then glued to the base plate. The vertical stabilizer is assembled with the same process, also with a servo integration plate but not yet glued to the plate. A dowel is put through the vertical stabilizer to help keep it together. The servos are then installed into the servo integration plates after the glue is dried. Then the control services were glued, ribs lined up with stringers. Plates are glued on the control surfaces in locations corresponding to the servo locations on the stabilizers. After all of them are dried they are covered by MonoKote. After all of them are covered, the rudder is glued to the base plate. With both stabilizers glued to the base plate, they are both glued to a T bracket for further stability. The control surfaces are then attached to the respective stabilizers with hinges and glue. Then the servos are connected to the control surfaces with a control rod. After the tail is finished, it is attached to the tail spar with two L brackets that are screwed to the spar and the base plate. All hardwood was glued with wood glue for its stability, and all balsa was glued with CA for its speed of assembly. The screws are bolted because the stress on them is relatively low.

§6.10 – Competition Mechanisms

Both the mission 2 and 3 mechanisms were mostly 3D printed. 3D printing was selected because of the complex geometry of the mission 2 racks and the mission 3 rack and pinions, which is extremely difficult to manufacture using other methods. An infill of 30% was selected after multiple prototypes were created, and this infill percentage allowed the parts to handle their loads while also being as lightweight as possible. These components also require a very small tolerance (i.e., mission 2 racks needed to have a very specific diameter that is small enough to tightly hold the syringes, but large enough to allow a team member to quickly load them in without much friction).

§7 – Testing Plan

§7.1 – Key Ground and Flight Tests

§7.1.1 – Mission 3 Pack*age Deployment Mechanism*

§7.1.1.1 – Finite Element Analysis

In order to quantify the sensitivity of structural characteristics on design considerations, a finite element analysis was performed to determine the maximum displacement, maximum Von-Mises stress, and maximum Von-Mises strain on the racks during each point in their operation. The models on which these simulations were performed were imported directly from their CAD files to ensure fidelity. ANSYS Student was used to perform this analysis.

The racks were simulated as being composed of ABS plastic, with fixed supports corresponding to the aircraft's ribs on their underside and forces equal to half the weight of each vaccine package distributed along the top of the teeth encompassed by each package's base. In the first case, three such loads were applied, and the number of loads was subsequently reduced by one per trial to simulate the dropping of the packages over the course of Mission 3. The locations of the loads and supports were also moved in order to model the different positions the racks would be in at each stage of the mission. Though the stress was high, hitting a few hundred kPa, the deflection and strain were insignificant as less than a micrometer of deflection would not affect the mission mechanism's performance. Images of the deformation are shown in Figure 7.1.1.1.1 below. The maximum deformation, stress,

and strain values for each case are listed in Table 7.1.1.1.1 In the tables, a) represents the deformation with one package, b) the deformation with two packages, and c) the deformation with three packages.

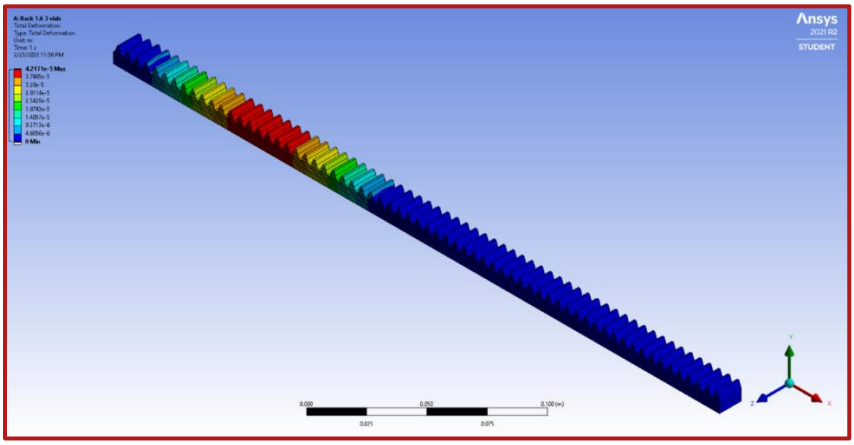

Fig. 7.1.1.1.1 ANSYS Rack Deformation for 3 packages

Table 7.1.1.1.1 Maximum Deflection, Stress, and Strains

Maximum Deflection, Stress, and Strains for Package Loading			
Number of Packages	**Max Deflection (μm)**	**Max Stress (kPa)**	**Max Strain (m/m)**
1	0.310	891.76	55.227×10^{-5}
2	0.793	316.56	2.281×10^{-5}
3	0.422	318.32	2.226×10^{-5}

§7.1.1.2 – Rack Load Test

A load test is conducted to determine if the racks could carry the load of the vaccine vial packages without deflection or failure, as specified in requirement MECH 6 and MECH 7. The racks were 3D printed using ABS plastic and 40% infill. ABS plastic was used because it is relatively easy and cheap to obtain, while also being lightweight at about 1.0 g/cm^3. Also, 40% infill allows the weight to be lower while maintaining the rack strength necessary to hold the vaccine vial packages without deflection.

Figure 7.1.1.2.1 shows the experimental setup, where boxes weighing 600g (which gives a factor of safety of 1.3 as the actual load for 2 packages is 460g) are placed on the racks, whose supports are 6.27 inches apart. The distance of 6.27 inches represents the greatest gap between two fuselage ribs, which provide structural support to the racks. This gives the location where failure is most likely to occur, assuming no inconsistencies in the material.

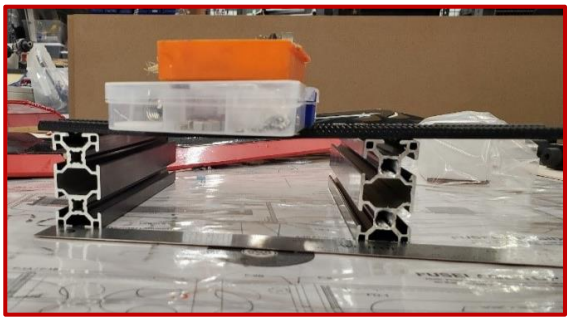

Fig. 7.1.1.2.1 Load Test Setup, with Racks and Weights Shown

The load test's results were recorded qualitatively and indicated non-significant levels of deflection, as seen in righthand side of Figure 7.1.1.2.1. This indicates that the current load could be supported.

§7.1.1.3 – *Container Drop Shock Sensor Test*

A drop test was conducted to determine the height at which the vaccine vial packages could be dropped safely, without triggering the 25G shock sensors. A prototype of the package was manufactured and is shown in Figure 7.1.1.3.1. The exterior frame was constructed out of wood to mimic the competition-given payloads. The inside was filled with other small items to bring the block's weight to about 8.00 oz. Each of the shock sensors were placed along the XYZ axes to ensure that the impact force would not be triggered in any of the three dimensions.

Fig. 7.1.1.3.1 Vaccine Vial Package Prototype with 25G Shock Sensors"

To further ensure the accuracy of our tests, a testing rig designed to mimic that which was present on our aircraft was constructed. This allows the vaccine vial package to be dropped consistently from the same height manner. It is designed to recreate the package sitting on racks, which are resting on channels in the fuselage ribs. The test rig is shown in Figure 7.1.1.3.2.

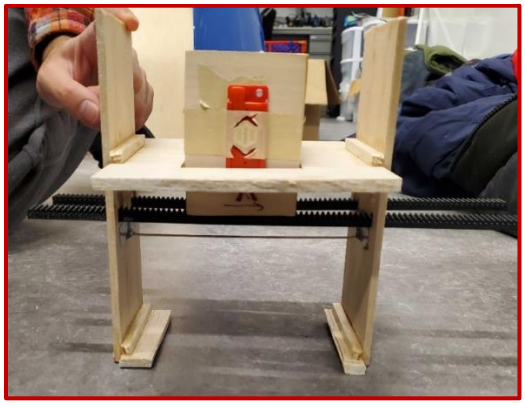

Fig. 7.1.1.3.2 Drop Test Rig, with Package Prototype, Racks, and Rubber Band Shown

The test rig's height was made to match the height at which the package would drop out of from the fuselage. To test, the racks were pulled by hand to drop the package at the normal height of 3.5 inches above the ground, and then also at 4, 4.5, and 5 inches onto a hard tile surface. The height of 5 inches gives a factor of safety of about 1.43. The packages were dropped 10 times for each height. The shock sensors were not triggered, except for one time with the vertically mounted sensor when dropped from 5 inches. With 100% success rates with a 3.5, 4, and 4.5-inch drop and a 90% success rate at 5 inches, as specified earlier in requirement MECH 7, it was concluded that the current vaccine dropping mechanism using a rack and pinion with a rubber band would likely be successful.

§7.1.1.4 – Ground Test

A ground test will be conducted to verify the overall functionality of the package dropping mechanism, as specified in requirement SYS 2, MECH 6, and MECH 7. First, the subsystem is integrated into the plane by slotting the racks into the fuselage rib holes and aligning them with the servo-driven pinion. The servo is then connected to the propulsion system for power. The vaccine vial package prototypes are then positioned on top of the racks. Finally, the transceiver was used to rotate the servo, which moves the racks and drops the packages. The shock sensors are then examined to ensure that they were not triggered.

§7.1.2 – Landing Gear Testing

The landing gear's steering and brakes functionality were tested using an ESC. The servos for each were confirmed to work and respond to commands appropriately. The aircraft was then placed on the ground and steered using controls, with the steering and brakes working as intended. The front wheel was determined to have a maximum steering angle of 20°, which surpassed our requirement of 10° in MECH 1. The brakes managed to stop the plane in around 20 feet, meeting the requirement of SYS 4.

The landing gear's maximum deflection was tested using a scale and physical loading forces delivered by pushing down with human hands. Tests were conducted on a piece of wood identical to the baseplate and nose plate of the fuselage, in order to observe how much force the baseplate, nose plate and each part of the landing gear could handle before breaking. During rear landing gear testing, the mock baseplate copy fractured after each test. However, during the front landing gear testing, neither the nose plate nor the front wheel broke, with each gear themselves holding up without any noticeable damage.

Separately, each gear was tested to observe the maximum deflection they could reach on their own. The maximum observed deflection was 1° for the front gear and 40° for each wheel of the back gear. The scale measured forces up to 60 N, but the deflection that was achieved was discovered far after the scale was overloaded. The front wheel did not break even under the maximum stress that was physically applicable, but the back gear bent and fractured under a large amount of stress. A new, identical back gear was constructed after the test. The force required to achieve this maximum deflection was very large and sustained, far surpassing predicted loading forces of 66.2 N, and is likely never going to be encountered during a flight, even during the roughest landings. The deflections encountered during shock testing never exceeded 15° for the back gear or 1° for the front gear. An image of the landing gear is shown below, with the front on the left and the back on the right.

Testing was also conducted to determine the deflection of each wheel of the landing gear during each mission. When the plane is held in the air and completely unloaded as shown in Figure 7.1.2.1a, the front gear experiences a deflection of 2°, the right wheel of the back gear gains a 6° deflection, and a 3° deflection occurs in the left wheel.

Figure 7.1.2.1 (a) Unloaded Aircraft, Held Up in the Air. (b) Empty Aircraft, on the ground

Next, when the plane is empty but on the ground, as seen in Figure 7.1.2.1b, the deflection for each wheel is 2° for the front, 15° for the right, and 3° for the left.

Figure 7.1.2.2a displays when the plane is loaded with syringes for Mission 2. The deflection of each wheel in this case is 5° for the front, 15° for the right, and 5° for the left.

Figure 7.1.2.2 (a) Aircraft Loaded with Syringes. (b) Aircraft Loaded with Packages

Lastly, when the plane is loaded with packages for Mission 3, as displayed in Figure 7.1.2.2b the deflection of each wheel is 15° for the front, 17° for the right wheel, and 7° for the left wheel. During testing, only one of the three packages for Mission 3 was available, so boxes of screws that also weighed approximately 8 oz were used as substitutes and placed in the right spots.

The deflection angles were larger than the ideal values but were not large enough to significantly concern the team. The large deflection angle for the front wheel likely came from the pole of the front landing gear being slightly smaller than the screw bracket connecting it to the servo, causing it to tilt slightly. The angle for the right wheel of the back gear likely was a consequence of repeated stress testing, which may have weakened the right side of the arch.

§7.1.3 – Fuselage Spar Finite Element Analysis

ANSYS Workbench was used to verify the structural integrity of the wing integration piece. This analysis was performed by transferring a SolidWorks assembly of the wing integration piece and the wing and fuselage spars into ANSYS workbench and assigning proper material values to each component. A Young's modulus of 228 GPa and Poisson's ratio of 0.22 was assigned for the braided carbon fiber and a Young's modulus of 10.1 GPa with a Poisson's ratio 0.022 for basswood. A 150 N force for both thrust and lift were applied to the wing Integration piece to examine the internal stress. This magnitude of force was chosen to ensure that the wing integration piece would be able to withstand the max thrust of the motors and then some. Forces of 7N and 15N were applied to their

respective positions along the fuselage spars to represent the weight of the battery and payloads respectively. As seen in Figure 7.1.3.1 most of the stress was loaded in the front spar of the fuselage with a max stress of 6.5 MPa, well within material limits for a composite of carbon fiber and epoxy which yields a yield strength of 745 MPa. The max stress within the wing iteration piece came out to be 6.5 MPa, also well within the material limits of basswood with a yield strength of 40.7 MPa. Through this analysis we were able to prove that our structure has a factor of safety of at least 6.2 times the expected loads.

As a worst-case scenario simulation, the loads of the payload and battery were doubled to 14 N and 30 N respectively to simulate a possible 2g pull that could be experienced in a 60-degree banked turn. As seen in Figure 7.1.3.2 the max stress in the carbon fiber spars came out to be 26.2 MPa and 18.1 MPa in the wing integration piece. These are once again well within the material limits of 745 MPa and 40.7 MPa. This proves that a worst-case scenario factor of safety of 2.2.

With these results it is safe to say that the carbon fiber spars, and wing integration piece shall hold up to any load it encounters. While it seems unreasonable for the team to have chosen carbon fiber for the wing and fuselage spars, these excessive factors of safety ensure that under no circumstances will the wing spar snap. The high material strength of the spars will also aid in minimizing the deflection of wings under loading [13] .

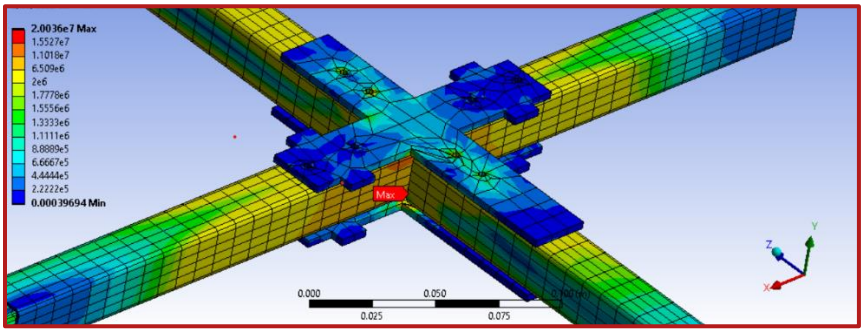

Fig. 7.1.3.1 ANSYS Stress Analysis Results of Wing Integration Piece and Fuselage Spar

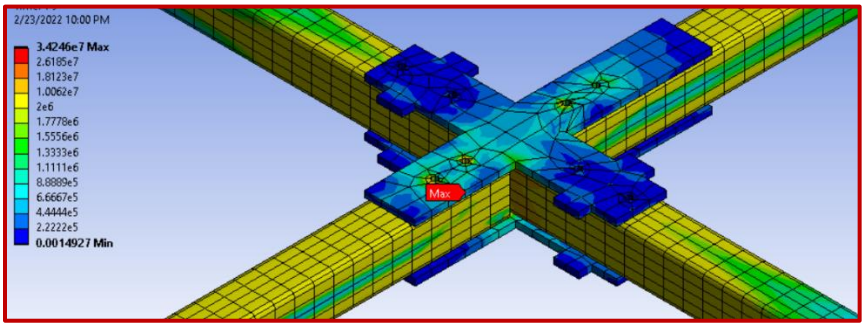

Fig. 7.1.3.2 ANSYS Stress Analysis Results of Wing Integration Piece and Fuselage Spars Under Double the Expected Load

§7.1.4 – Wingtip Loading and Deflection

The team carried out a wingtip loading test to ensure the plane's wings can support the loads during the three missions while under maximal stresses due to factors such as turns or turbulent air.

§7.1.4.1 - Modeled Deflection

Before carrying out the actual test, the team modeled the stresses the wing is under with the expected load (1g) and with the factor of safety (3g) by treating it as a beam bending problem. For this model, the wing can be approximated to the combination of the two carbon fiber spars because they are the only connection between the wing and the fuselage, so the spars serve as the primary load-bearing component in the wing. The team also assumed the load due to the mass of the aircraft to be applied at the center of the wingspan where the two spars connect because the distribution of the wing's weight can be considered negligible compared to the weight of the entire aircraft. For both the model and actual test, the team used the highest payload, which was Mission 2 (4.616 kg), to gauge the maximum deflection possible in the spar. In terms of dimensions, each carbon fiber spar is 4 feet long for a combined length of 8 feet (2.4 m). The cross-section of both spars is square with an outer length of 0.9 inches (2.3 cm) and inner length of 0.75 inches (1.9 cm). The Young's Modulus of Elasticity of the spars is 61.5 GPa. The deflection was modeled using the Maximum Deflection Equation 37, which also required using Equation 38 for calculating the second moment of area. The deflection results for both the expected load and factor of safety were then plotted in MATLAB according to the Elastic Curve Equation 39 [13].

$$\Delta_{max} = \frac{pL^3}{48EI} \tag{37}$$

$$\mathrm{I} = \frac{bh^3 - b_1h_1^3}{12} = \frac{b^4 - b_1^4}{12} \tag{38}$$

$$\Delta = \frac{p}{48EI}(4x^3 - 3L^2x) \; for \; x \leq \frac{1}{2}L \tag{39}$$

§7.1.4.2 - Physical Test

To carry out the actual test, the aircraft was filled with the Mission 2 payload. Two members of the team lifted the aircraft from both wingtips and held a string to each wingtip at roughly the point of the center of gravity along the chord (to simulate a roughly 2.5g load case) and the deflection of the wing root was measured through the difference in height of the spar and a string attached to both ends of the wingtips using a ruler temporarily attached to one wing, as shown in Figure 7.1.4.2.1. This satisfies the AERO 2 requirement.

Fig. 7.1.4.2.1 Holding Airplane With Maximum Payload Up With Wingtips

§7.1.4.3 – Wing-Spar Integration Bracket Stress Analysis

To further justify our design for the Aluminum bracket, we conducted a stress analysis using the ANSYS Engineering Simulation Software. Each motor produces 18N of thrust force, meaning that each bracket experiences 9N of force

at the location of the 2 lower screw holes, in the downward direction, with respect to the figure below. We, however, applied a significantly greater force of 30N to each bracket, to account for the motor thrust force, the motor's weight, and any insignificant force(s) present. Fig. 7.1.4.3.1 shows the results of the stress analysis simulation. The maximum stress shown in the analysis is well under the 240 MPa yield strength of the Al 6061-T6 material.

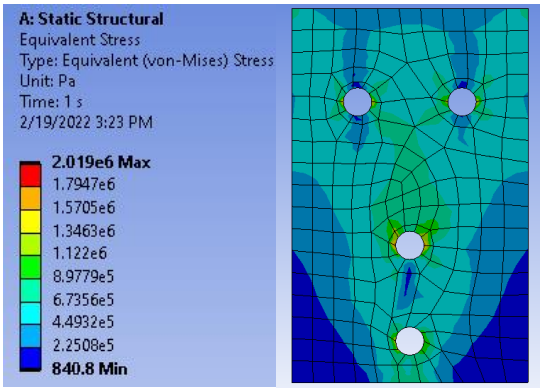

Fig. 7.1.4.3.1 ANSYS Stress Analysis Simulation

§7.1.5 – Propulsion Tests

§7.1.5.1 – Static Thrust Test

Static thrust testing served two reasons: to verify the values derived from eCalc simulations, and to ensure that sufficient thrust was available for stable flight of the aircraft for ten minutes. Thus, when the propulsion combination in section 5.1 was selected, a static thrust test rig was assembled using the same components. Tests at 100% power for take-off and at 90% power for cruise were performed. Figure 7.1.5.1.1 shows the set-up of the testing rig.

Fig. 7.1.5.1.1 Static Thrust Testing Rig.

In Fig. 7.1.5.1.1 the propeller and motor are mounted on a rotating L-bar of equal length, with the other end placed on top of an electronic scale. As the motor spins, the propeller will apply a thrust force on the L-bar, generating a moment about the pivot point. This moment is counteracted by the normal force by the electronic scale, which will read out the normal force being supplied. Since the L-bar is of equal length, the scale reading will be equal to the amount of thrust being generated. As this year the propulsion system was a twin motor, the team decided to perform multiple static tests. The motors were individually tested, and static thrust data points were summed to give an approximate combined static thrust.

§7.1.5.2 - Motor Mount Structural Test

A motor mount structural test was conducted to ensure the motor mount can withstand the stresses induced by the aircraft's thrust, as specified in requirement PROP 3. Should the mount fail, the thrust generated by the motor could inflict significant damage to the aircraft. To ensure that the mount does not break, a piece of twine was hung from the screw that will hold the mount with the spar, as well as the holes that will hold the motor. As each motor was estimated to provide 19.7 N of force, the twine was loaded with 3 kg of force, allowing for a factor of safety of around 1.5. Figure 7.1.5.2.1 below shows the setup of the test.

(a) (b)

Fig. 7.1.5.1.2 Motor Mount Setup.

Fig. 7.1.5.1.2a shows twine laced over the screw inserted into the motor mount and wrapped around the handle of a bucket full of sand. Bucket and sand have combined mass of 3kg. Fig. 7.1.5.1.2b demonstrates the lacing used to secure twine to test the other side of the motor mount in the same fashion as Fig. 7.1.5.1.2a.

Table 7.1.5.2.1 Requirements and Tests

Test Name	Static Thrust	Motor Mount Structural	Propulsion Analysis	Wing Tip Loading	Control Surface	Low Speed Taxi	High Speed Taxi	Fuselage Analysis	Landing Gear	Mission Two Ground	Mission Three Ground	Deployment Flight	Mission Two Flight	Mission Three Flight
Req #	PROP: 2	PROP: 3	PROP: 1 4	AERO: 1 2	AERO: 3	MECH: 2	MECH: 2	SYS: 1 2 MECH: 3 4 5	MECH: 1	SYS: 1 MECH: 3 5	SYS: 2 MECH: 4 5 6	SYS: 3 4 5	SYS: 1 3 4 5	SYS: 2 3 4 5 6 MECH: 6 7

§7.2 – Timeline and Schedule

Due to unavoidable circumstances that arose during the assembly process, most ground and flight tests were shifted back a couple of weeks. The static thrust test needed to occur in order for taxi tests or flight tests to happen. While the motor was being configured, other mechanical tests were able to occur without the need of a full system operation. These tests include a landing gear deflection / steering test, M3 rack and pinion ground testing, a fuselage assembly roll test, wingtip deflection testing, and other simple structural tests.

After the propulsion system was finalized and tested, flight tests were able to occur. However, a significant factor in the delay of flight tests became suboptimal weather conditions. Only about one of the many days in a week became a convenient day to fly our aircraft, but time was especially of the essence since the aircraft had to be completely

ready for flight the morning of. As we proceeded in the testing process, the consequences of delaying one test becomes apparent as many tests build upon previous testing over time. As a result, the flight tests and mission specific ground tests are in progress currently.

§7.3 – Checklists

The following checklist is used by the team to ensure safety and preparedness for flight tests.

Task	✓	Remarks
Electrical Power Sources		
Verify Main Propulsion Battery at full charge		
Verify Receiver Battery at full charge		
Verify Transmitter Battery at full charge		
Aeronautics		
Verify wings are well secured to the fuselage		
Identify location of center of gravity		
Wingtip test		
Actuation		
Zero servos		
Correct servo connections to receiver, battery and ESC		
Ensure servos are securely fastened		
Verify control surfaces have enough deflection		
Propulsion		
Ensure correct propeller is mounted		
Ensure propeller is securely fastened		
Ensure we are using a Right (not Left) propeller		
Miscellaneous Tests		
Landing Gear/Roll Test		
Propulsion Mount Structural Test		
Transmitter Range Test		
Record total prop weight and total plane weight		
Flight Contingency Case Manifest		
LiPo Protective Bag		
Electrical Tape, Duct Tape, Hinge Tape		
Scissors, Xacto Knives (2)		
Hand Drill and Drill Bits		
CA Glue (2, Instant and Gap Filling) and Extra Tips		
Balsa sheet (⅛, 1/16), balsa stringers		
Extra Transmitter, Receiver, ESC		
Thermal Blanket for Cold Weather		
2x sets of Allen Keys		
Bolts and Nuts		
Logistics		
Ensure weather conditions favorable		
File for FAA approval		

Pre-Takeoff Checklist

Task	✓	Remarks
50% Throttle, Throttle Closed, Full Up Elevator, Full Right Rudder, Full Right Aileron		
Radio Failsafe set, Arming plug in possession		
Propeller rotating in correct direction		
Favorable Wind, Weather Conditions		

§8 – Performance Results

§8.1 - Static Thrust Testing

The team performed static thrust testing on the testing rig for each individual motor to accurately measure how much thrust was available for take-off, as well as to compare theoretical results from the eCalc software. For each motor, a 6s XILO 2250mAh battery and Talon 25A ESC were used. Table 8.1.1 shows the results of the tests:

Table 8.1.1 Static thrust testing results

Motor	Motor Model	Propeller Diameter (in)	Propeller Pitch (in)	Measured Static Thrust (kg)	Predicted Static Thrust (kg)
Left	Cobra CM 4012/30	13	9	1.509	1.870
Right	Cobra CM 4012/30	13	9	1.610	1.870
Total	-	-	-	3.119	3.740

Table 8.1.1 shows that the static thrust test was relatively accurate compared to eCalc predicted thrust generated. Note that the measured static thrust does not consider external factors, such as inefficient force transfer onto the balance of the rig and manufacturing tolerances. It is also expected that the thrust will be greater than the measured static thrust when the aircraft is in motion.

§8.2 - Wingtip Deflection Testing

The team performed a wingtip deflection test both through modeling the bending of the carbon fiber spar and physically by holding up the wingtips to measure the amount of deflection that the actual wings. For the test, the deflection associated with Mission 2's load (the mission with the highest payload) was measured. Table 8.2.1 (below) shows the results of both the modeling and test and Figures 8.2.2 and 8.2.3 show the results of the 2 modeled beam deflections.

Table 8.2.1 Wingtip Deflection Test

Wingtip Deflection Test			
Load	**Load (N)**	**Modeled Deflection (cm)**	**Observed Deflection (cm)**
Expected load (1g)	45.24	1.89	2.75 in = 7.0 cm
Factor of safety of 3	135.71	5.66	

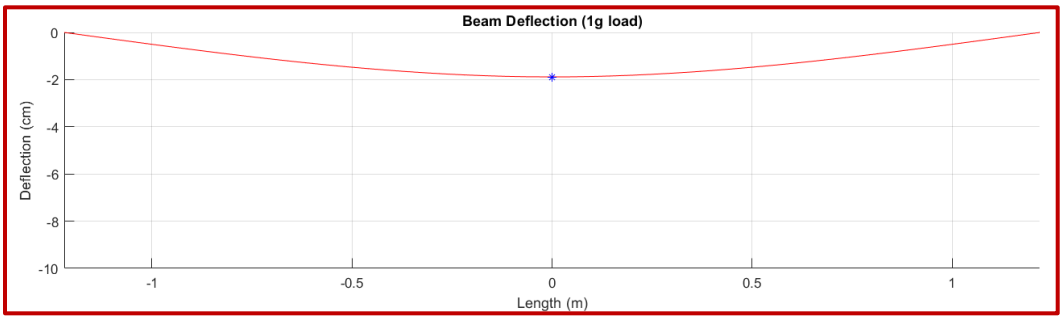

Fig. 8.2.2 Graph of Modeled Deflection with 1g load

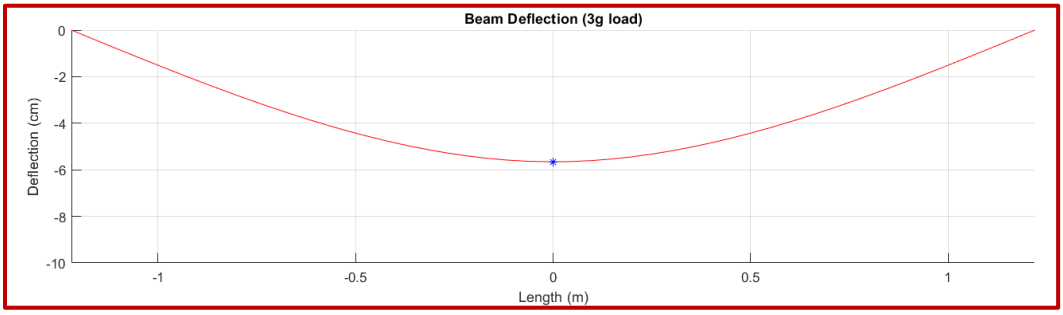

Fig. 8.2.3 Graph of Modeled Deflection with factor of safety (3g)

§8.2.1 - Analysis

The observed deflection was much greater than the modeled deflection. One possible reason for this is that the spar is not fully integrated into the fuselage, leading to some rotation of the spar. The two spars were integrated by attaching them with four screws into the hardwood plate of the fuselage. However, the screws were inserted with different depths and only attached the components from the top of the fuselage. The wing spar splice where the two spars connect also may not perfectly hold the spar together inside the fuselage as rigidly as one 8 foot spar. Therefore, the spars may have been able to rotate upwards during the test with the connection point tilting downwards due to the weight of the fuselage. This would cause the deflection of the beam to appear larger for the given force applied at the wingtips. The splice and screws of different lengths could also cause one side of the wing to bear slightly more of the aircraft weight, which could make the spars appear to deflect by different amounts depending on where the string height is measured.

References

[1] *2021-2022 Design, Build, Fly Rules*, American Institute of Aeronautics and Astronautics, 2021. URL https://www.aiaa.org/docs/default-source/uploadedfiles/aiaadbf/dbf-rules-2022.pdf.

[2] Sadraey, M. H., *Aircraft Design: A Systems Engineering Approach*, Wiley, 2012. URL https://onlinelibrary.wiley.com/doi/book/10.1002/9781118352700.

[3] Raymer, D. P., *Aircraft Design: A Conceptual Approach*, American Institute of Aeronautics and Astronautics, Inc., 2018.

[4] "Airfoil Tools Database," *unknown*, unknown. URL airfoiltools.com.

[5] *UIUC Airfoil Coordinates Database*, UIUC Applied Aerodynamics Group, 2022. URL https://m-selig.ae.illinois.edu/ads/coord_database.html.

[6] Raymer, D. P., *Aircraft Design: A Conceptual Approach*, American Institute of Aeronautics and Astronautics, Inc., 2018.

[7] Gudmundsson, S., "GENERAL AVIATION AIRCRAFT DESIGN: APPLIED METHODS AND PROCEDURES," 2014. https://doi.org/http://dx.doi.org/10.1016/B978-0-12-397308-5.00001-5.

[8] Drela, M., *Athena Vortex Lattice (AVL) Software*, Massachusetts Institute of Technology, 2020. URL http://web.mit.edu/drela/Public/web/avl/.

[9] Backer, W. D., and Muhawe, V., "Mission definition, Analysis of Requirements, Concept Selection and Fuselage Design," 2009. URL https://www.academia.edu/4229218/04_FUSELAGE_DESIGN.

[10] Keane, A. J., Sobester, A., and Scanlan, J. P., *Small Unmanned Fixed-Wing Aircraft Design. A Practical Approach*, 2017.

[11] AeroToolbox, "Horizontal and Vertical Tail Design," 2021. URL https://aerotoolbox.com/design-aircraft-tail/.

[12] Finck, R. D., "USAF Stability and Control DATCOM Final Report," *Fink, R.: USAF Stability and Control DATCOM.. AFWAL-TR-83-3048. McDonnell Douglas Corporation, Douglas Aircraft Division, for the Flight Controls Division, Air Force Flight Dynamics Laboratory, Wright-Patterson AFB, Ohio. October 1960, revised November 1965, revised April 1978.*, 1978.

[13] DeWolf, J. T., Mazurek, D. F., Jr, E. R. J., and Beer, F. P., *Statics and Mechanics of Materials*, McGraw-Hill Education, 2021.